Final Report

a. DE-FG02-01ER45934
Case Western Reserve University

b. "Nanoscopic Manipulation and Imaging of Liquid Crystals"
Charles Rosenblatt

c. Date of report: February 4, 2014
Period Covered: September 15, 2001 through November 14, 2013

d. Accomplishments

The project's goals centered on nanoscopic imaging and control of liquid crystals and surfaces. We developed and refined techniques to control liquid crystal orientation at surfaces with resolution as small as 25 nm, we developed an optical imaging technique that we call Optical Nanotomography that allows us to obtain images inside liquid crystal films with resolution of 60 x 60 x 1 nm, and we opened new thrust areas related to chirality and to liquid crystal/colloid composites. Below is a topic-by-topic detailed discussion of project results.

Spatially homogeneous writing In order to increase the switching speed of a LC display, it often is desirable for the director $\hat{n}$ to be *slightly* tilted by an angle θ_0 with respect the perfectly vertical (or perfectly planar) alignment directions, where θ_0 is called the "pretilt angle" and typically is less than 2^o. But what happens when pretilt angles are much larger? If an angle of, *e.g.*, $\theta_0 = 10^o$ or even 45^o were feasible, would new physical phenomena appear? Could one exploit such large pretilt angles for new applications? The answer to these questions is "yes." However, it first is necessary to *create* a large and robust — both temporally and thermally — LC pretilt angle and to understand the physics and chemistry that lie behind it. This was an early goal of my DoE-supported grant.

The most common method of achieving planar alignment is by deposition of a polyimide on a substrate and unidirectional rubbing with a cotton cloth [1]. Rubbing has two consequences: the creation of grooves that promote alignment of the liquid crystalline molecules [2] and, more importantly, a reorientation of the polyimide backbone, which results in epitaxial alignment of the LC by means of anisotropic dispersive interactions [3]. Alternative approaches [4,5,6,7,8] for achieving planar alignment include exposure of a polymer-coated substrate to polarized ultraviolet light, targeting a hard substrate with an ion beam, and oblique deposition of SiO. Despite great strides, however, these methods still are commercially used far less frequently than mechanical rubbing with a rolling cotton cloth.

Vertical alignment may be achieved by deposition of a monolayers of a long chain-length silane or a surfactant [9], or by deposition of a polyimide that has a long side group. Working with the commercial material SE-1211 (Nissan Chemical Industries, Ltd., Fig. 1), we demonstrated that baking at a higher temperature and for a longer period of time than recommended by the manufacturer results in a large, controllable, and temporally robust (at least many months)

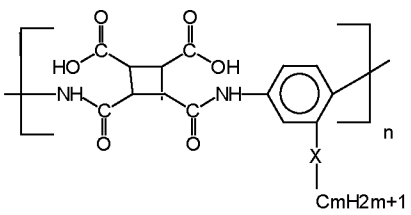


Fig. 1 Material SE-1211

pretilt angle, where the pretilt angle $0 < \theta_0 < 50^o$. ($\theta_0 = 0$ corresponds to vertical alignment) [10]. This "overbaking" has two important consequences: additional imidization of the backbone, which is elongated by the mechanical rubbing, and a cleaving of some of the side groups, diminishing the propensity of the polyimide to induce vertical alignment in the liquid crystal.

During the course of the grant we made a number of investigations aimed at elucidating the mechanism(s) behind this phenomenon and exploiting it for possible applications. Building on our initial work, we created a cell designed to provide a large pretilt angle θ_0 in the nematic phase, but filled the cell with a liquid crystal that possesses not only a nematic phase, but a smectic-A phase as well. Our goal was to determine whether the presence of surface-induced smectic order would drive the surface orientation of the liquid crystal from a nonzero θ_0 deep inside the nematic phase toward $\theta_0 = 0$ on cooling toward the nematic – smectic-A transition. Quantitative analysis of the data requires a topographically uniform substrate, as well as an extremely spatially uniform interaction potential. As standard rubbing techniques involving a rubbing cloth do not meet these requirements, we turned to AFM writing of the substrate to achieve excellent homogeneity. Using four different writing strengths (given by the stylus force), we obtained the data shown in Fig. 2 [11]. As expected, harder scribing was found to induce a larger pretilt well above the nematic – smectic-A transition temperature T_{NA}. Moreover, the second order tilt transition (from $\theta_0 \neq 0$ to $\theta_0 = 0$) on cooling occurs closer to T_{NA} for harder scribing. This is because a larger degree of surface-induced smectic layering is required to compensate for the stronger tilt, and this occurs closer to T_{NA}. Based on these results we proposed a model that involves *two* preferred orientations ("easy axes"), one approximately vertical and one approximately planar, for LC alignment, with the equilibrium value of θ_0 determined by competition between these two directions. These experimental results, however, do not rule out a single, but tilted, easy axis that changes with temperature.

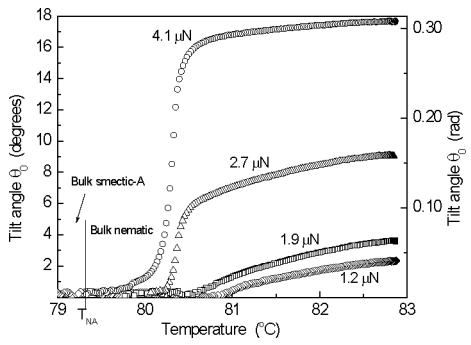


Fig. 2 Tilt angle *vs.* temperature for Merck liquid crystal SCE12R at different scribing strengths.

Multiple Easy Axes We then asked the question: Is there a measurement that could distinguish unambiguously between the single and dual easy axes mechanisms? The answer is "yes": a measurement of the polar anchoring strength coefficient[1§] [12] W_2^{θ} *vs.* θ_0. If the LC director $\hat{n}$ adopts an equilibrium polar orientation θ_0 at the interface, but is forced to deviate from this orientation due to an elastic torque and/or an electric field, there exists an energy cost F_{int}. It turns out that the coefficient $W_2^{\theta} \propto \theta_0^2$ for the dual easy axis model, but W_2^{θ} is approximately constant in the single (but tilted) easy axis picture. We performed the first simultaneous measurements of W_2^{θ} and θ_0 [13], and indeed have found the "smoking gun," *viz.*,

§ The free energy associated with deviations from the equilibrium surface orientation (θ_o,φ_o) is given to lowest order by $F_{int} \approx \frac{1}{2}W_2^{\theta}\sin^2(\theta-\theta_o) + \frac{1}{2}W_2^{\varphi}\sin^2(\varphi-\varphi_o)$+ higher order terms [12], where θ and φ are polar and azimuthal angles, and θ_o and φ_o are the orientations of the "*effective* easy axis" for the director. In the dual easy axis picture, the "effective easy axis" is the equilibrium orientation determined by the two physical easy axes. Note that W_2^{φ} is a function of θ_0, vanishing for vertical alignment. We define $\theta_o = 0$ as perfectly vertical alignment. Note that $\theta_o \neq 0$ implies a nonzero "pretilt" angle at the substrate. "Weak anchoring" implies small values of W_2^{θ} and/or W_2^{φ}, and thus a large susceptibility for reorientation from the effective easy axis by an external force.

W_2^{θ} is proportional to θ_0^2 (Fig. 3). The LC very definitely interacts with *two* easy axes at the substrate.

Controlled Pretilt We have examined several other aspects of homogeneous pretilted anchoring. We found, for example, that the threshold rubbing strength n_{th} — this applies to both rubbing with a cotton cloth and scribing with an AFM stylus — required to induce nonzero pretilt in the LC increases with increasing alkyl chain length of the LC [14]. For glass coated with the silane surfactant dimethyloctadecylaminopropyl trimethoxysily chloride (DMOAP), Chen, et al observed more complete wetting of longer alkyl group homologs of the liquid crystal alkylcyanobiphenyl than of the shorter homologs [15], indicating the importance of the liquid crystal's alkyl chain length in promoting homeotropic order. Now consider our SE-1211 alignment layer (Fig. 1), which consists of long alkyl side chains that promote nearly homeotropic orientation and a polyimide backbone that, when aligned, tends to promote nearly planar alignment. For strong rubbing the backbone becomes sufficiently aligned, allowing the liquid crystal to overcome the homeotropic alignment tendency due to the side chains. But the propensity for homeotropic order is related to the length of the liquid crystal tail, and thus for longer LC molecules the rubbing must be stronger to overcome the enhanced homeotropic tendency of longer chain mesogens. Thus, the threshold rubbing strength n_{th} to induce a nonzero pretilt increases with increasing liquid crystal tail length, as seen in Fig. 4.

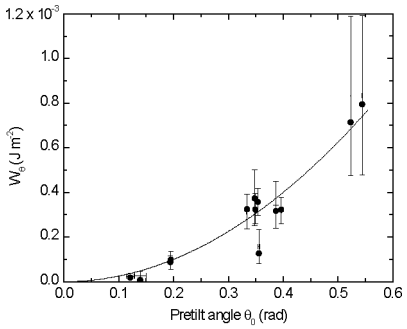


Fig. 3 Anchoring strength *vs.* pretilt angle, showing quadratic behavior.

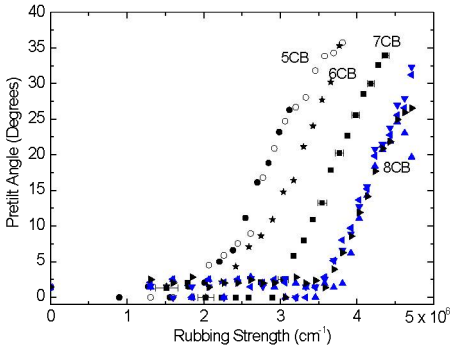


Fig. 4 Pretilt angle vs. rubbing strength for four homologs of the series alkylcyanobiphenyl.

Having demonstrated the existence of two easy axes [13], we examined the behavior of the director pretilt angle as a function of temperature above the smectic-A – smectic-C transition at the LC – substrate interface [16], wherein the substrate is prepared with the polyimide SE-1211 to induce pretilt in the nematic phase. We found that the LC director is tilted even in the higher temperature smectic-A phase, where the tilt diverges on cooling toward the transition temperature. This implies that a nonzero torque exists, which could only come about if the two easy axes are not quite orthogonal.

Surface Polarizations In a very different sort of experiment, we demonstrated that for a nematic phase composed of chiral molecules, there exists a polarization situated at the interface and oriented perpendicular to the molecular tilt [17]. The experimental geometry is shown in Fig. 5. As described above, a polar pretilt angle θ_0 was imposed at the two substrates using the polyimide SE1211. A spatially homogeneous LC director orientation in the bulk was

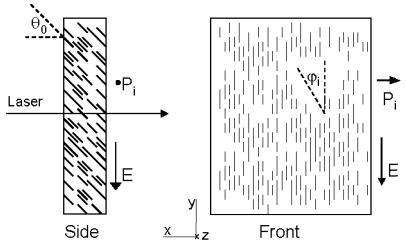


Fig. 5 Side (a) and front (b) views of experimental cell.

obtained by orienting the two substrates such that the pretilt directions are parallel, as shown in Fig 5a. On symmetry grounds [18] we suggested that an interfacial polarization P_i must exist at the two surfaces when the LC molecules are chiral. In order to detect the polarization, an in-plane a.c. electric field E at angular frequency ω [applied by two in-plane electrodes that are not shown] couples to P_i, resulting in a torque on the director at the substrates. The director orientation in the interior of the cell can elastically follow the interfacial director rotation φ_i at low driving frequencies, but its response falls off at higher ω. An example of $d\varphi_i/dE$ *vs.* ω using the chiral liquid crystal mixture SCE12 (Merck) is shown in Fig. 6, where the polar tilt angle $\theta_0 = 9.2^o$ at $T = 89^oC$. We measured the response $d\varphi_i/dE$ as a function of frequency and temperature, from which we proved the existence of the proposed surface polarization effect, and extracted the polarization and anchoring strength coefficient W_2^{φ} as a function of the tilt angle at the substrates.

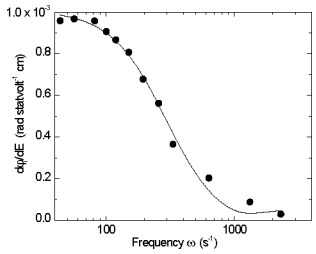


Fig. 6 $d\varphi_i/dE$ *vs.* ω for SCE12

First Order Freedericksz Transition The Fréedericksz transition plays an important role in both the science and technology of liquid crystals, and serves as the basis for the ubiquitous twisted nematic LC display. The Fréedericksz effect involves a tradeoff between elastic forces, which tend to minimize spatial variations of the director, and electric or magnetic forces that are applied to induce an elastic distortion. Below a threshold field E_{th} the elastic forces win, and the LC adopts an undistorted director profile; for $E > E_{th}$ the director profile undergoes a distortion. Ordinarily this is a second order transition, although it was suggested theoretically [19] that the confluence of three conditions will cause the transition to become first order: very thin cells, LC-substrate interactions with a large negative quartic term in the surface free energy expansion [20], and a LC having a bend elastic modulus that is much larger than the splay value. We have created such an environment, and demonstrated experimentally the first order nature of the transition and how it varies with cell thickness [21].

Spatially inhomogeneous Nanoscribing Several years ago we modified our AFM to facilitate the writing of spatially *inhomogeneous* patterns, such as herringbone patterns for planar alignment, patterned topographies, and patterned variations in the polar pretilt angle θ_0 [22]. This opened up a host of new possibilities, in that we now are able to investigate phenomena such as phase transitions and wetting in which the characteristic length scale of the pattern can be of the same order as, or smaller than, the correlation length associated with the LC order parameter, as well as new technological devices such as optical gratings.

In my original demonstration of substrate-induced smectic order at a smooth substrate above the nematic – smectic A phase transition [23], the Fréedericksz threshold field of a nematic cell was observed to increase anomalously on cooling close to the transition. The observed increase, over and above that expected from the divergence of the bend elastic constant K_{33}, was the result of difficult-to-deform smectic layers growing at the substrate. With the advent of nanoscopic control of surface topography, we have examined the effect of a nanoscopically *rough* surface on surface-induced smectic order [24]. One surfactant-coated substrate was scribed locally with the AFM stylus to create a nanoscopic grooved structure (See Fig. 7). This roughness had the effect of decreasing the surface-induced smectic order parameter in the nematic phase, as predicted by Mirantsev [25], with a resulting



Fig.7 Surface topography created by AFM scribing of surfactant alignment layer. Period is 250 nm.

decrease in the Fréedericksz threshold field E_{th}. By measuring E_{th} as a function of temperature in both scribed and unscribed regions of the cell, we were able to examine the effects of surface roughness on the growth of smectic layers, as well as extract the bare smectic correlation length.

Melting at a Patterned Surface About twenty years ago Barbero and Durand [26] showed that if the nematic liquid crystal director attempts to follow the topography of a rough surface, the associated curvature elastic energy cost may result in a decrease of the order parameter near the surface, or even result in melting of the LC into the isotropic phase. Several qualitative results for rough surfaces subsequently have been reported [27,28]. In contrast to surface topography, one also may examine elasticity-induced melting by patterning the surface with a planar easy axes whose direction varies with position. To quantify the effects on the isotropic – nematic transition temperature T_{IN} due to a nanoscopically-varying planar director profile, we scribed a herringbone pattern into a polyimide-coated substrate that induces planar alignment [29]. Each period of 200 nm (along the x-axis) contained two very long pixels, approximately 100 nm wide (along the x-axis) and 100 μm long (along the y-axis). The pixels were scribed so that their easy axes made angles of $+\psi/2$ and $-\psi/2$, respectively, with respect to the y-axis, where values of ψ (the angle between adjacent easy axes) were chosen over the range $15^o \leq \psi \leq 88^o$. The depression of T_{IN} at the patterned surface relative to its value at a uniformly-oriented surface was investigated as a function of ψ. Figure 8 shows a sequence of images of the nematic wetting layer front on approaching the herringbone region. In this sequence, a temperature gradient is imposed, with the dark region in each frame corresponding to a higher temperature than the colored (nematic wetting layer) region. From left to right the spatially-averaged temperature in each image is reduced, but the gradient is held constant. The phase front first reaches the edge of the scribed square at temperature T_1, then envelopes (but does not invade) the herringbone-scribed region due to the extra elastic and anchoring energy costs in that region, and then finally at temperature T_2 the elasticity and anchoring energy costs no longer can prevent the nematic wetting layer from appearing over the square. The quantity $\Delta T \equiv T_1 - T_2$ was measured as a function of angle, and is shown in Fig. 9. In conjunction with the Kelvin equation we were able to calculate the thickness (30 ± 5) nm of the nematic wetting layer [30]. Additionally, the results indicate that anchoring — rather than elastic — effects play the dominant role in the suppression of the transition temperature.



Fig.8 Sequence of images showing the progress of the nematic wetting layer front, as it envelopes then finally breeches the herringbone-scribed region. Note that the absolute position in each image is shifted slightly so that the wetting front is placed in the center of each image.

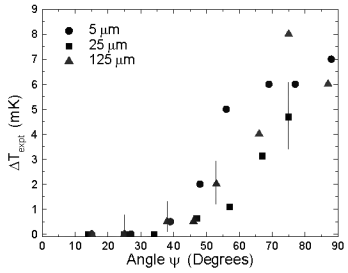


Fig. 9 Depression of T_{NI} *vs.* angle between scribe lines ψ. The nematic appears as a thin wetting layer of thickness ~ 30 nm, and therefore the data are independent of the overall thickness of the sample. Results from three sample thicknesses are shown.

Spatial Control of Anchoring Let me return to the issue of pretilt angle control. For scribing of polyimide SE-1211 weaker than the threshold strength n_{th}, vertical alignment of the LC ($\theta_0 = 0$) is maintained, but the polar anchoring strength is reduced from its value in the unrubbed case. In fact, the anchoring strength vanishes at a scribing strength just below n_{th}. An interesting and important consequence of anchoring is that the threshold voltage for a Fréedericksz transition is smaller for the finite anchoring case than it is for the case of infinite

anchoring, and vanishes when the anchoring coefficient W_2^{θ} at the two substrates goes to zero. Thus, one may tailor the optical properties of a LC device by controlling the anchoring properties. To demonstrate this concept we coated a glass substrate with Nissan Chemical Industries polyimide SE-1211, and then divided a 50 x 50 μm pixel into "subpixels" consisting of stripes of width 5 x 50 μm (Fig. 10). The even numbered stripes were left unscribed, and thus produced vertical alignment with strong polar strong anchoring conditions. The odd numbered stripes were scribed, but not strongly, with lines spaced 100 nm apart; thus θ_0 remained zero but the polar anchoring was weak. Using a negative dielectric anisotropy LC that aligns *perpendicular* to an applied electric field, we applied a field normal to the substrates [31]. Above a first threshold field the LC in the weakly anchored subpixels underwent a Fréedericksz transition, with a characteristic brightness *vs.* voltage curve when illuminated by polarized light that passed through a crossed polarizer before entering the detector. At a higher field a second Fréedericksz transition occurred, this time in the unscribed subpixels. The overall brightness *vs.* voltage characteristics of the entire pixel consisted of the sum of the two, and displays a distinctive step, as seen in Fig. 11. Calculations were performed that mimicked the observed behavior quite well [32]. Ultimately, control of surface interactions will allow us to create a device with a step-wise brightness *vs.* voltage curve, and have a significant impact on the driving circuitry of an LCD.

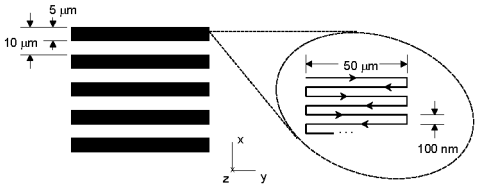


Fig. 10 Scribing pattern for subpixels.

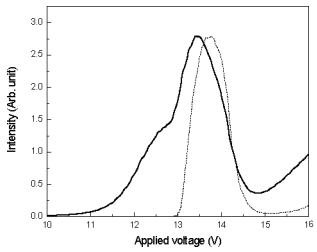


Fig. 11 Brightness *vs.* voltage curve for pixel divided into scribed and unscribed subpixels. The dashed line represents a region that has not been scribed. Notice that the step in the solid line occurs at the Fréedericksz threshold voltage for the unrubbed curve.

Simple Optical Grating Along a completely different line, we have been exploiting our ability to write patterns in order to create a variety of optical gratings. Some of these were described in the previous proposal, and are outlined in Ref. [33]. As part of our work, however, we have created a *polarization-independent,* electrically switchable blazed grating. This grating takes incoming light of any polarization and, in the voltage-off state, directs the beam into a single diffraction spot. In the voltage-on state the beam passes straight through the grating, undiffracted. The grating is based on the our ability to tailor spatially the polar pretilt angle, where a single period is divided in three or more subpixels. The tilt angle in each subpixel is chosen such that the optical retardation for one optical polarization varies stepwise from 0^{o} to approximately 360^{o} — it can be as low as 240^{o} and still be quite efficient (Fig. 12). This pattern then repeats over and over. We have devised a way to handle both states of polarization simultaneously; thus the polarization of the light is not important in the overall throughput. Figure 13 shows two images of the beam — the left image is in the voltage-off diffracting state (currently about 85% efficiency into the desired diffraction spot) and the

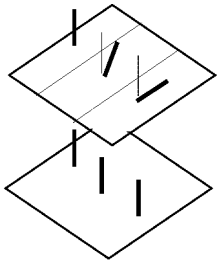


Fig. 12 Schematic representation of director pattern at the two substrates when pixel is broken into three subpixels.



Fig. 13 Voltage-off state (diffracting state) left; voltage-on state (nondiffracting) right. The bright and dim diffraction spots in the left-hand panel correspond to the desired first order peak at -θ and a small undesired peak at +θ, respectively. Note that the main (undiffracted) beam intensity is virtually zero in the voltage off state.

right image is in the voltage-on non-diffracting state.

Quartic terms in the smectic tilt susceptibility [34]. Several years ago we showed that controlled rubbing of the overbaked polyimide SE-1211 (Nissan Chemical Industries) facilitates a tilt of the LC director away from the vertical orientation in a nematic liquid crystal [35]. This occurs because the overbaking breaks off a fraction of the side chains that ordinarily promote vertical orientation, and further imidizes the polymer backbone. If there is a smectic-A phase nearby, we discovered that a surface-driven LC director tilt transition can occur [36] in the nematic, such that the "pretilt angle" θ_0 — I define this as the angle made by the director with respect to the substrate normal — goes continuously to zero on cooling toward a temperature T_a, which typically is several degrees Celsius above the nematic – smectic-A transition temperature T_{NA}. In this experiment we performed Freedericksz transition measurements on the Merck *racemic* liquid crystal mixture SCE12R in the region $T_{NA} < T < T_a$. On measuring the transmitted optical intensity we found that the Freedericksz threshold voltage is smallest just below T_a and increases with decreasing temperature. This indicates that the usual *quadratic* anchoring strength coefficient W_2 is very small near T_a and increases on cooling due to the onset of surface-induced smectic layering. More interesting, however, is the very slow increase of optical intensity with increasing voltage (above the Freedericksz threshold) throughout this temperature region. This latter effect is due to the contribution from the *quartic* anchoring coefficient W_4, which has the effect of suppressing large tilts above the Freedericksz voltage threshold. By examining the behavior of both W_2 and W_4 as functions of temperature — both scale as $(T-T_{NA})^{-3\nu}$, where ν is the correlation length exponent — we concluded that the molecules' resistance to tilt in the surface-induced smectic layers involves not only the quadratic coefficient, but depends critically on beyond-quadratic terms as well.

The Diverging nematic surface electroclinic effect at temperatures just below the tilt transition temperature T_a [37]. We prepared a cell similar to that in item *a* (above), except that this new cell was filled with the *chiral* version of the liquid crystal SCE12 (Merck). As above, over the temperature range $T_{NA} < T < T_a$ the liquid crystal exhibits vertical alignment (pretilt angle $\theta_0=0$), where T_{NA} is the nematic — smectic-A transition temperature. Because of the reduced symmetry at the substrate owing to the liquid crystal chirality, application of an in-plane electric field for $T_{NA} < T < T_a$ induces a nonzero polar tilt $\theta_0 \propto E$ of the LC director at the interface [38], where the tilted orientation propagates elastically into the bulk. On heating, this surface nematic electroclinic response becomes large, and diverges at T_a, the temperature that corresponds to the onset of a surface tilt transition from $\theta_0=0$ to $\theta_0\neq0$. We performed optical retardation measurements as a function of temperature and frequency of the driving voltage, and extracted the surface electroclinic coefficient (corresponding to the inverse anchoring strength coefficient $1/W_2^{eff}$), demonstrating divergent behavior at the tilt transition temperature T_a (Fig. 14).

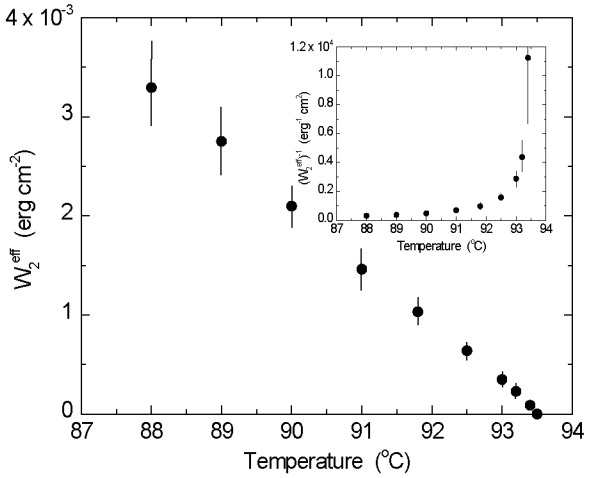


Fig. 14 Effective quadratic anchoring strength coefficient W_2^{eff} *vs.* temperature. Notice that W_2^{eff} vanishes at tilt transition temperature T_a. Inset shows $1/W_2^{eff}$

Planar degenerate alignment. A micro- or nanopatterned planar-aligned cell ordinarily requires a pair of mirror-image patterned substrates that must be aligned in register to less than 1 μm. This is very difficult! As an alternative we have examined the director orientation profile of a nematic liquid crystal in a cell composed of one substrate whose easy axis is patterned on small length scales λ (~ a few microns) and a second substrate treated for planar degenerate alignment using polymethyl methacrylate. For cell thickness < λ, we showed that the experimentally measured director profile in the bulk corresponds approximately to that imposed at the micropatterned substrate [39], in good agreement with theoretical calculations.

We investigated the **molecular organization of the polyimide SE-1211**, which is employed as alignment layers in LC displays, by means of vibrational Sum Frequency Generation (SFG) Spectroscopy [40]. We focused on the orientation of the long alkyl side groups at the polymer surface using polarization-selected SFG spectra of the CH_3- and CH_2-stretch modes of the side chain. We found that mechanical rubbing and baking, a procedure that we have shown produces controlled pretilt of the liquid crystal, induce a pronounced azimuthal anisotropy in the orientational distribution of the alkyl side chains. Orientational analysis of the SFG vibrational spectra of the alkyl side chains shows their preferential tilt to be along the rubbing direction, with the azimuthal distribution narrower for stronger rubbed polymer samples.

Pretilt control <u>using mixtures</u> of polyimides. As noted above, an important component of our work has been the control of polar pretilt angle. Our earliest work involved overbaking and rubbing the polyimide SE-1211 [35], as discussed briefly in item *a* above. Mechanical rubbing, however, tends to produce a less spatially-uniform pretilt than desired. As a result, we examined *mixtures* of the vertically-aligning SE-1211 polyimide and the planar-aligning RN-1175 polyimide (Nissan Chemical industries); the latter does not possess a side chain. We found that for a fixed concentration ratio 25 wt-% (SE-1211) : 75 wt-% (RN-1175), the polar pretilt angle θ_0 could be varied continuously over a nearly 90^o range from vertical to planar alignment by adjusting the baking temperature [41]. Moreover, using phase detection atomic force microscopy, which is sensitive to the local chemical composition of the surface, we showed that no microphase segregation of the two species was taking place. This is in contrast to the results of the Hong Kong University of Science and Technology group, which observed microphase segregation of their two materials and suggested that such segregation actually is required to obtain an average polar tilt in the bulk liquid crystal [42]. The absence of microphase segregation in our samples provides a much more uniform director orientation throughout a given pixel. But more importantly, we went on to show that at a fixed baking temperature the pretilt angle is a function of the relative concentration of the two polyimides [43]. This presents the intriguing possibility of using techniques such as ink-jet technology, where the "inks" correspond to the different polyimides, to deposit a controlled concentration at each pixel and thereby control the pretilt angle pixel-by-pixel.

Polarization-independent switchable optical grating. Over the years we have applied our nanocontrolled alignment technique to create devices such as optical gratings [44] and microdisplays [45]. We recently developed another grating architecture, which has the advantage of being independent of the optical polarization [46]. As before, the polyimide SE-1211, when overbaked and rubbed unidirectionally, induces a controlled polar pretilt angle in the liquid crystal. If rubbed weakly, however, a LC with negative dielectric anisotropy will adopt a

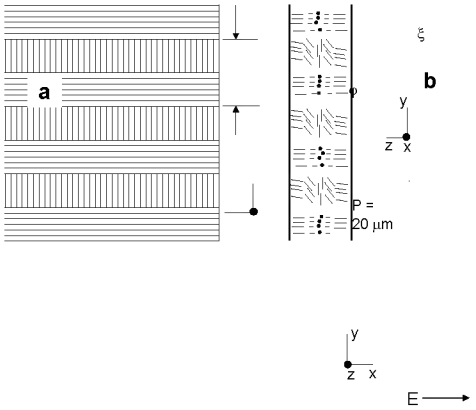


Fig. 15 (a) Front view: schematic diagram of rubbing pattern on one substrate. Each pixel is 10 μm wide, and φ represents the azimuthal scribing direction (0° or 90°). (b) Side view: (cross-section) of cell. ξ represents the electric field coherence length, such that the director in the bulk is approximately perpendicular to E for distances from the substrates >ξ. Note that figure does not show the azimuthal homogenization of the director away from the rubbed substrate.

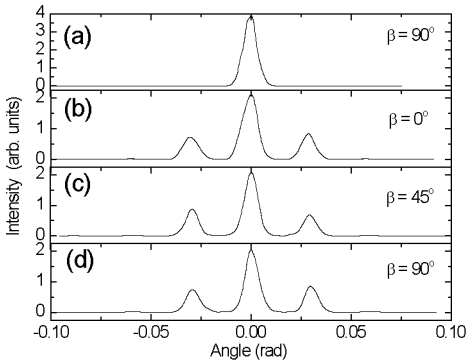


Fig. 16 (a) Intensity vs. angle for E=0. Only the central peak, m=0, is present. (b), (c), and (d) Intensity vs. angle for three different orientations β of the polarizer. Temperature T=40°C and applied voltage V=40 V rms. Efficiency *e* is independent of β. Note the decrease of the central peak m=0 intensity from the field-off case (a) due to diffraction, especially into the m=1 peaks

vertical orientation, but on application of an electric field perpendicular to the substrates, the director will undergo a polar tilt with azimuthal orientation along the rubbing direction. We used an atomic force microscope to scribe SE-1211-coated substrates to create an electrically-controlled polarization grating (Figs. 15, 16, 17). The grating is nondiffracting in the voltage-off state and diffracting in the voltage-on state, and its *efficiency is independent of optical polarization*. The grating may be prepared for diffraction in either one or two dimensions (Fig. 17).

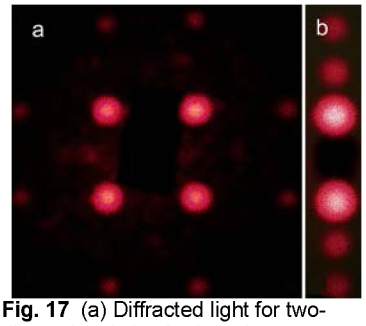


Fig. 17 (a) Diffracted light for two-dimensional checkerboard pattern (m=0 central peak is blocked out). Notice the presence of weak higher order peaks. (b) Diffracted light for the one-dimensional pattern (with central peak blocked out)

Expulsion of bend deformation from the smectic-A phase and the superconducting Meissner effect. Similarities between the superconducting and the smectic-A phases were noted by DeGennes in 1972 [47]. In particular, he showed that twist and bend deformations are expelled in the smectic-A phase, in analogy with the superconducting Meissner effect in which a magnetic field is expelled completely for a type I superconductor (Ginzburg parameter $\kappa < 1/2^{1/2}$) or partially, *i.e.*, with magnetic vortex penetration, for a type II superconductor ($\kappa > 1/2^{1/2}$). The Ginzburg parameter κ is the magnetic penetration depth (or, for the smectic-A phase, the bend or twist penetration depth) divided by the order parameter correlation length. In this experiment we performed measurements in the smectic-A phase in the temperature range $T_{NA} - T < 200$ mK for well controlled bend deformations created by AFM scribing of a polymer substrate [48]. In this temperature region (close to T_{NA}) the correlation lengths are sufficiently large relative to the penetration depth that the smectic-A phase is of type

I. In consequence one expects melting into the nematic phase to occur in regions of high bend curvature, which is precisely what we observed. We coated one substrate with a planar-aligning polyimide and scribed three herringbone easy axis patterns using our AFM. The three patterns had half-angles of $\gamma = 10^{o}$, 15^{o}, and 20^{o} between the rubbing directions in adjacent pixels. The opposing substrate was coated with polymethyl methacrylate which, as we showed in item *c* above, induces planar degenerate alignment [49]. Polarized optical microscope images were recorded on slow heating toward T_{NA}. Very close to T_{NA} the width of the high curvature regions (near the apexes of the herringbone) that melt into the nematic phase were observed to grow in size, and the profile of optical intensity *vs.* position across the interface was deconvoluted to obtain the actual width L of the melted nematic region (Fig. 18). This width L was found to increase with increasing temperature toward T_{NA}, and was several μm in extent for $T_{NA} - T \sim 10$ mK. The results are in excellent agreement with our scaling model [48] based on DeGennes' theory for the width of the melted nematic region for a type I smectic [50].

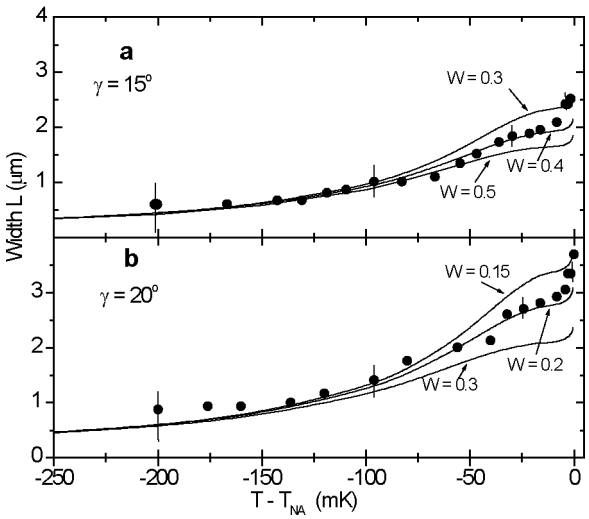


Fig. 18 Width L of bend-induced melted nematic region *vs.* temperature in the smectic-A phase for two different herringbone angles. Solid lines represent our scaling theory based on DeGennes' model. The only unknown parameter is the quadratic anchoring strength coefficient W_2 (in erg cm^{-1}). Theoretical prediction for several values of W_2 are shown.

Director uniformation at the nematic – smectic-A transition in a nanopatterned cell. We examined a cell that was nanoscribed with herringbone patterns of various wavelengths, but this time images were collected on *cooling* toward the nematic – smectic-A phase transition temperature from above T_{NA} [51]. The patterns serve as a template for alignment of the liquid crystal octyloxycyanobiphenyl (8OCB) and, as discussed above, impose a bend distortion in the liquid crystal in the vicinity of the herringbone apexes. The pretransitional behavior of the LC was observed by polarized microscopy, allowing the direct visualization of the growing (near T_{NA}) temperature-dependent extrapolation length, which is related to the tradeoff between elastic and anchoring forces. Just above the phase transition temperature T_{NA} we observed the expulsion of bend deformation (except very close to the herringbone apexes; see item *g* above), behavior that we showed to be in good quantitative agreement with continuum theory. Additionally, very close to the transition temperature T_{NA} we observed an interesting weak threshold behavior. For short spatial periods the bend distortion is expelled completely, with the director field adopting a uniform bulk configuration (Fig. 19). For long spatial periods, however, the smectic breaks into domains that are separated by curvature walls (Fig. 19). The observed behavior is

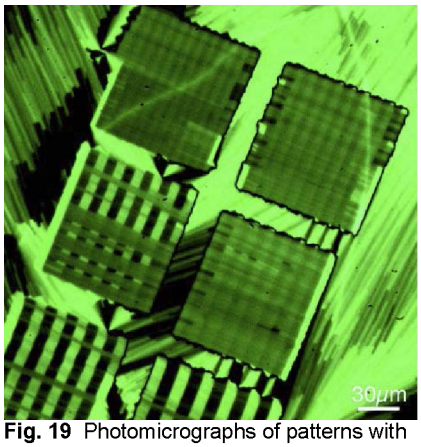


Fig. 19 Photomicrographs of patterns with different periods, just below T_{NA}

consistent with a mechanism for which the director pattern becomes locked in at a critical temperature $T_c > T_{NA}$ at which the smectic correlation length grows to be the same order as the associated extrapolation length. If at this temperature the extrapolation length is much smaller than half the herringbone period, multiple domains obtain; in the opposite limit a monodomain appears.

Optical nanotomography of anisotropic fluids. The physical properties of anisotropic fluids can be manipulated on very short length scales of 100 nm or less by appropriate treatment of the confining substrate(s). This facilitates the use of ordered fluids, such as liquid crystals, in a variety of applications ranging from displays to switchable optical elements such as gratings and lenses. Owing to diffraction limitations, high resolution three dimensional imaging of the liquid crystal's molecular orientation profile has been beyond the reach of extant optical techniques. Instead, we have developed a powerful new imaging approach ("Optical Nanotomography"), which is based on the use of polarized light emitted from a tapered optical fiber, to investigate molecular orientation in three dimensions at nanoscale levels [52]. We immersed the fiber's tip inside a thin layer of liquid crystal that sits atop a substrate and raster-scanned the fiber at a series of heights above the surface (Fig. 20). [Several experiments have demonstrated that the fiber's perturbative effect on a nematic liquid crystal is very weak. These will be discussed in the Proposed Work]. From the images collected in the far field we obtained a three dimensional visualization of the liquid crystal's structure with a resolvable volume two to three orders of magnitude smaller than attainable by extant methods such as confocal microscopy. We demonstrated this technique by examining a nematic liquid crystal whose director orientation is controlled by a nanoscopic pattern scribed into the underlying polyimide-coated substrate. We were able to image the extrapolation length ~ 200 nm — this is much smaller than that in item *h* because there is no nearby smectic-A phase — over which the molecular orientation relaxes due to the liquid crystal's elastic forces. Moreover, the "fingers" at the right in each of the images in Fig. 20 are due to the topography of the substrate created by the AFM-scribing, such that the optical retardation of the LC measured from the fiber aperture to the substrate varies with the surface topography. From the relative contrast in each image, a peak-to-peak surface height variation of 17 ± 3 nm was determined, in excellent agreement with the value of 18 nm determined by a non-contact AFM topographical measurement [53]. This technique of acquisition and analysis of image slices offers the intriguing possibility of 3D nanoscale reconstruction of a variety of other soft materials.

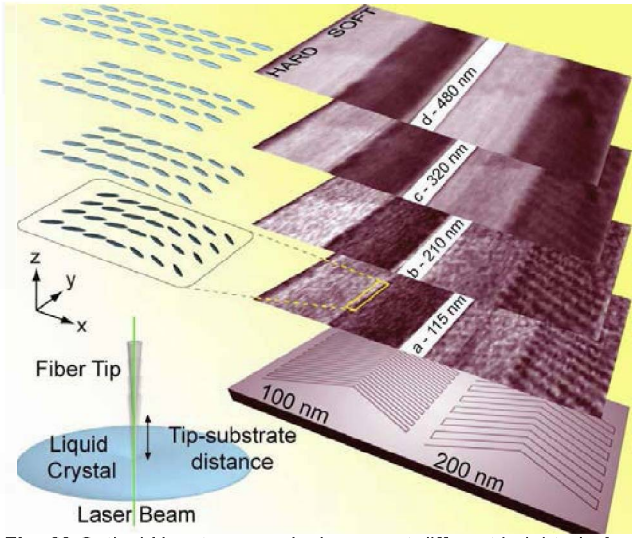


Fig. 20 Optical Nanotomography images at different heights *h*. A series of images created from the intensity data matrix collected at heights (a) 115 nm, (b) 210 nm, (c) 320 nm, and (d) 480 nm above the polymer coated substrate, with an uncertainty of ± 10 nm. The scan dimension is approximately 15 x 9 μm. Polarizer makes an angle β nominally equal to 7.5° and 37.5° with respect to the easy axes. Note the "fingers" in the images on the right.

Direct measurement of surface-induced nematic order S(z). The conventional approach [54] to surface-induced orientational order in the isotropic liquid crystal phase involves a delta-function (*i.e.*, a highly localized) interaction potential between the substrate and liquid crystal, which induces nonzero nematic order S_0 at the substrate above the bulk transition temperature T_{NI}. For sufficiently weak S_0 the order decays approximately exponentially into the bulk, although for stronger surface order the higher order terms — proportional to S^3 and S^4 in the Landau expansion of the free energy — need to be included and can give rise to prewetting and capillary condensation phenomena [55,56,57]. In this experiment we treated the substrate for weak planar order by means of weak rubbing. We then used a variation on our Optical Nanotomography technique by keeping the optical fiber fixed in the *x,y*-plane but varying its height *h* above the substrate [58] and measuring the intensity I(h) downstream. In the present experimental configuration the intensity *I* is proportional to the integrated birefringence when the variation in *h* is small (<100 nm), and thus proportional to the integrated nematic order parameter S(z) from the substrate to the fiber's aperture at height *h*. Thus the quantity dI/dh allows us to extract S(z) with resolution ~ 1 nm normal to the interface. We collected data as a function of aperture height *h* and temperature ΔT above T_{NI}; I show the resulting values of S(z) in Fig. 21. The results indicate that for weak order, the inverse susceptibility at the wall (S_0^{-1}) is linear in $T - T_{NI}$; this is consistent with weak surface order ($S_0 < 0.12$) and no capillary condensation, as expected. But much more importantly, S(z) does *not* decay exponentially with *z*, but rather falls off weakly for the first 5 – 8 nm, and then decays rapidly (Fig. 21) further from the substrate. This behavior is contrary to all extant results, both theoretical and experimental, in which a delta-function surface potential and exponential decay have been *assumed*. In collaboration with Elena Pikina (Oil and Gas Research Institute, Moscow), we showed theoretically [59] that the small value of the nematic-isotropic (NI)-interfacial tension results in the renormalization of the repulsive interaction potential due to the thermal fluctuations of the soft NI-interface. This leads to an increase of the equilibrium width of the induced nematic region and the appearance of a step-like orientational order parameter profile, as seen in Fig. 21. We found that only renormalized short-range and thermal pseudo-Casimir interactions are essential for this behavior.

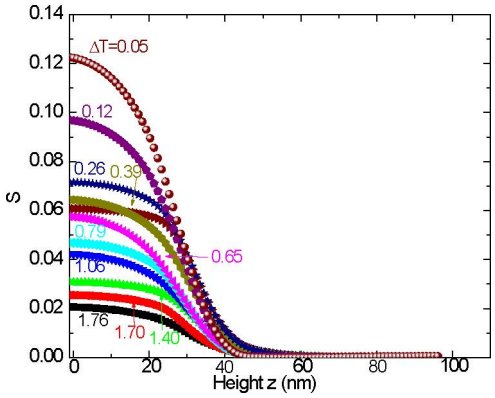


Fig. 21 Nematic order parameter S(z) at different temperatures. Note that Bezier curves were fitted to the raw data, which in turn were differentiated to obtain these results.

Direct visualization and measurement of the extrapolation length Owing to the liquid crystal's elasticity, the director is unable to follow sharp changes in azimuthal orientation φ that are imposed by a substrate patterned for spatially-varying alignment. The "extrapolation length" *L* corresponds to the distance over which the director is able to change orientation, and is given by $L = K/W_2$, where *K* is an appropriate elastic constant and W_2 is the "anchoring strength coefficient" for deviations φ from the local patterned "easy axis" direction, *i.e.*, to lowest order the anchoring free energy $F_s = \frac{1}{2}W_2\varphi^2$. *L* often is of order 100 to 300 nm, and until this work, had been measured only indirectly. Using our technique of optical nanotomography (ONT) [**Error! Bookmark not defined.**], we have made a direct visualization and measurement of *L* [60] on cooling the liquid crystal toward the nematic – smectic-A phase transition temperature T_{NA}. We found that *L* exhibits a sharp increase just above T_{NA}, quantitatively consistent with the

known critical behavior of the bend elastic modulus [61].

Observation of stripe texture due to nanoscribing We observed [62] a striped texture that appears in a twisted nematic (TN) cell when the "easy axis" for the alignment of the director is created by means of *bi*directional scribing of one of the polyimide-coated substrates using an AFM stylus [Fig. 22]. These striped textures [Fig. 23], which are visible when observed under crossed polarizers and correspond to a modulation of the director twist through the cell, do not occur in typical TN cells in which both substrates are prepared by *uni*directional rubbing. That stripes having multi-micrometer spatial periods appear when one substrate is treated by bidirectional AFM scribing — the scribed lines are ≤ 200 nm apart and their orientation makes an arbitrary angle with the stripes — indicates the action of an indirect mechanism between the scribed surface and the stripes. The observed phenomenon, along with the topography of the polyimide surfaces, suggests the breaking of mirror symmetry at the surface, resulting in surface (quasi-2D) chirality. Here "surface chirality" is defined as the inability to superpose an object onto its mirror image by rotation and translation within a plane; the letter "F" is chiral in 2D, whereas the letter "E" is achiral.

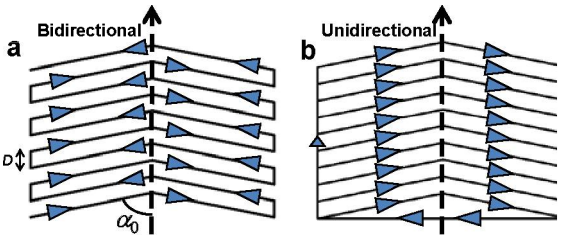


Fig.22 Bidirectional and unidirectional scribing using the stylus of an atomic force microscope.

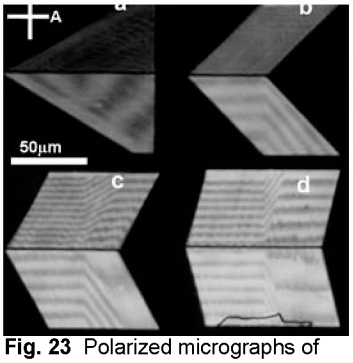


Fig. 23 Polarized micrographs of stripe patterns.

Chiral nanopatterning of substrates Based upon the previous result, we embarked on a vigorous program to design and create chiral surfaces mechanically. Moreover, we devised an electrooptic experiment utilizing a liquid crystal as a probe to determine unambiguously whether our nanoscopically bidirectionally-scribed alignment layer [Fig.22] is, indeed, chiral. To demonstrate the surface chirality of the alignment layer, we placed a planar-aligned negative dielectric anisotropy achiral nematic liquid crystal (methoxybenzylidene butylanaline) in contact with the mechanically generated chiral surface and applied an electric field E normal to the surface [63]. We found that the nematic director exhibits an "electroclinic effect", wherein the director undergoes an azimuthal rotation $\theta \propto E$ and gives rise to an optical signal linear in E [Fig. 24(a)]. This electroclinic effect is a clear signature of chirality of the alignment layer. (It is important to note that this chirality exists even in the absence of the liquid crystal; the liquid crystal is used solely as a probe.) Importantly, the electroclinic effect was *not* observed [Fig. 24(b)] when the polyimide was treated for a centrosymmetric topography, and therefore the surface was nonchiral. This electrooptic technique, moreover, provides a method for

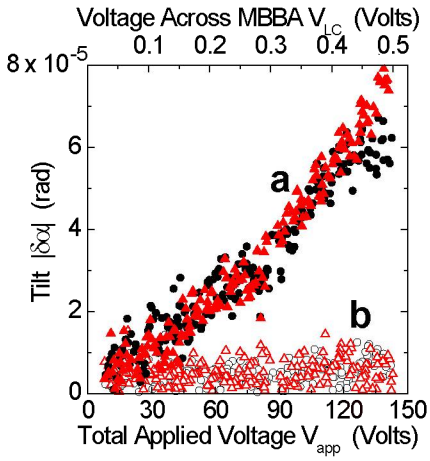


Fig. 24 Experimental electroclinic effect for a) chiral surface, shown by closed symbols; and b) an achiral surface, shown by open symbols. Note that the signal does not vanish at zero voltage, as the lock-in amplifier was operated in R/θ mode. Circles (black) correspond to data on increasing the voltage with time, and triangles (red) correspond to decreasing the voltage with time. No hysteresis was observed.

determining the relative strength of the chirality through the magnitude of the electroclinic effect. Thus, using purely mechanical means, we have mechanically generated a chiral surface that has consequences at the molecular level.

Our next goal was to create surface chirality with *controlled chiral strength*. To that end we coated a substrate with an achiral polyimide alignment layer and scribed unidirectionally with the AFM stylus, using a periodic line-to-line force profile $F_AF_BF_CF_AF_BF_C\ldots$ [64]. This produces is a non-centrosymmetric topography that, along with a vector associated with the cantilever, forms a two dimensional basis with no mirror symmetry. We then fabricated a cell using this substrate and a nonchiral opposing substrate, and filled the cell with an achiral liquid crystal. The strength of the resulting chiral surface was examined using the electroclinic effect induced at the chiral surface. Measurements were made by holding the ratio F_A:F_B:F_C at 3:2:1, but by varying the multiplicative force prefactor κ (Fig. 25, which shows surface roughness). The magnitude of the electroclinic effect was found to increase with increasing scribing force, which suggests a highly-reproducible method for controlling the chiral strength.

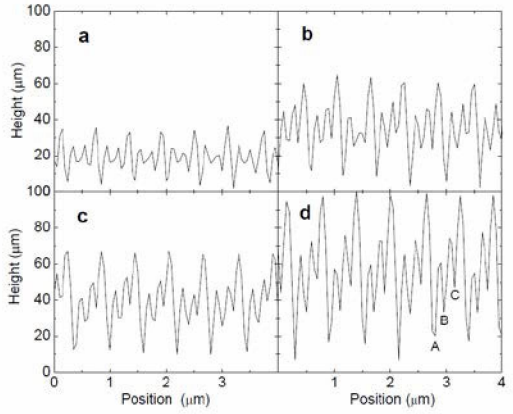


Fig. 25 Topographical cross sections for the four force prefactors κ. The corresponding rms roughnesses are R_{rms}=8.1, 12.4, 14.0, and 23.3 nm. Note the non-centrosymmetric pattern

We then used our AFM to scribe a chiral *step* pattern into a polyimide alignment layer, obtaining exquisite control of the chiral strength by varying the steps' length-to-width ratio R, Fig. 26 [65]. We exploited the same electrooptic effect to measure the chiral strength $d\theta/dE$, which turns out to be nonmonotonic in R: $d\theta/dE$ is zero for $R = 1$ (as expected on symmetry grounds), it reaches a maximum in the vicinity of $R \sim 6$, and tends to zero as $R \to \infty$. The maximum chiral strength occurs when the "chiral cores", *i.e.*, the jogs in the pattern, are separated by a distance comparable to twice the nematic extrapolation length L.. This behavior suggests that the chiral cores interact up to a separation $2L$, beyond which the spatially-averaged chiral strength decreases, as the density of chiral cores $\propto 1/R$. Our results demonstrate that chiral handedness and strength can be precisely controlled mechanically on nanoscopic length scales, and in principle can be varied spatially over the surface.

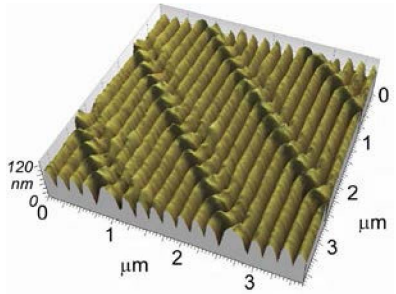


Fig. 26 AFM topographical image of scribed step pattern with ratio R = 8

Top-down chiral induction Since antiquity chiral phenomena always had been "bottom – up", where the chiral constituents, such as molecules, give rise to chiral-specific macroscopic behaviors such as the macroscopic twist distortion associated with cholesteric liquid crystals, circular dichroism, optical rotatory power, and systemic effects of chiral pharmaceuticals. Here we approached chirality from the opposite direction: A macroscopic torsional strain was used to induce conformational deracemization of the configurationally achiral molecules [66]. To accomplish this, we imposed a macroscopic helical twist on an achiral nematic liquid crystal (having a phenyl benzoate core) by rotating the azimuthal easy axis of one substrate with respect to the other. On application of an electric field the director was

observed to rotate in the substrate plane. This effect, which requires the presence of chirality, is strongest at the two substrates, increases with a tighter imposed helical pitch, and depends strongly on the liquid crystal – surface interaction. Our model involves a trade-off among bulk elastic energy, surface anchoring energy, and entropy associated with molecular deracemization, suggesting the imposed director twist induces a deracemization of chiral conformations of the molecules — effectively ‘‘top-down’’ chiral induction — quantitatively consistent with our experiment. In a follow-up experiment we added a chiral dopant to the liquid crystal to compensate *approximately* for the elastic cost of the imposed twist. By varying the dopant concentration around this compensation point, we unambiguously demonstrated [67]: i) the chiral electrooptic effect is localized very close to the two surfaces, ii) the electrooptic effect vanishes when the mixture’s “natural” rotation across the cell gap equals the imposed twist of the cell, and iii) by determining the thickness of the cell at which the twist is exactly compensated by the chiral dopant , we can determine accurately the helical twisting power (HTP) of the dopant / liquid crystal combination.

Periodic mesoporous organosilica (PMO) Periodic mesoporous organosilicas (PMO) are prepared by the surfactant-templated condensation of bridged organosilsesquioxane monomers. By controlling the nature of the organic segment, the type of surfactant and the condensation conditions, one can control the physical and chemical properties of the resulting PMO and produce highly ordered porous structures with a periodicity on the nanometer scale. The development of chiral PMO materials has been of significant interest given their potential in heterogeneous asymmetric catalysis, chiral chromatography and non-linear optics [68,69,70]. To date, characterization of the chirality of pore structures in these materials had been achieved by indirect methods including polarimetry [71] and solid-state circular dichroism [72]. In this project we probed the pore structure of chiral PMO materials based on their interactions with liquid crystalline solvents [73], which result in the induction of measurable chiral properties in the nematic and smectic A phases of the liquid crystals. The templated co-condensation of a biphenylene organosilsesquioxane monomer and a chiral binaphthyl organosilsesquioxane monomer produced a new chiral PMO material that we investigated as a dopant in two different liquid crystal hosts. We conducted measurements of induced circular dichroism and helical pitch in the nematic phase of the liquid crystal pentylcyanobiphenyl (5CB), and the measurement of an induced electroclinic effect dθ/dE in the smectic-A phase of the phenyl benzoate liquid crystal 9OO4 (Fig. 27). The induced chiral behavior measured in these experiments is consistent with chirality transfer taking place inside the pores, and suggests that the inner structure of the pores in the PMO material is indeed chiral and can induce chirality in a configurationally achiral liquid crystal.

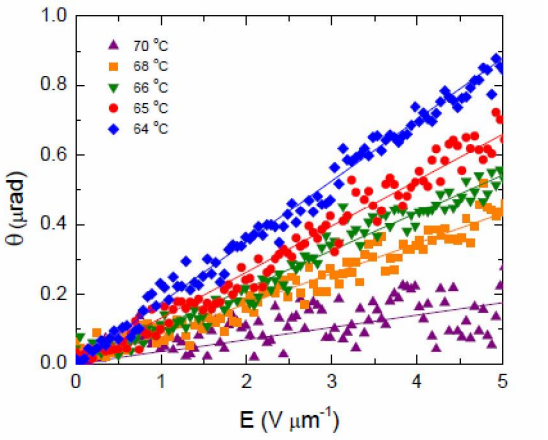


Fig. 27 Electroclinic effect measured as the spatially-averaged amplitude of the tilt angle vs. electric field in smectic-A phase of 1 wt.-% mixtures of (S)-15-QPMO1-ex in 9OO4

Carbon nanotube / liquid crystal mixtures We have conducted extensive investigations of multiwalled carbon nanotubes (CNTs) in liquid crystal matrices. In our first experiment, we dispersed a small quantity of multi-walled carbon nanotubes in an achiral liquid crystal with a thioester in the core, and the mixture was found to exhibit a small degree of

chirality [74]. The induced chirality in the liquid crystal was probed in the smectic-A phase, which showed mean-field like pretransitional behavior on approaching the smectic-A –smectic-C transition temperature from above. The resulting electroclinic coefficient *vs.* temperature has a shape identical to that of a bulk chiral liquid crystal, although it is many orders of magnitude smaller, due in part to the relatively small concentration of chiral nanotubes. From the data we surmised that the chirality is transmitted a distance of a few nanometers into the bulk liquid crystal, and that what should have been a racemic mixture of chiral nanotubes actually has a weak enantiomeric excess of ~ 0.01. Interestingly, we observed that the effect is even much smaller if the liquid crystal has an oxoester rather than thioester core [75].

Electrooptic measurements of CNTs in the nematic phase also exhibit a bulk-like response [76], with an even smaller magnitude than in the smectic-A phase. Most importantly, though, is that the variation of the electroclinic coefficient with frequency is negligible over the frequency range 100 Hz – 100 kHz in the nematic phase well above the smectic-A transition temperature T_{NA}, whereas the electroclinic coefficient falls off significantly with increasing frequency just above T_{NA}. An analysis involving the characteristic response times for the bulk and surface electroclinic effects and the smectic correlation length(s) suggests that the chiral induction length is ~ 5 nm, consistent with atomistic modeling by Berardi, *et al* [77].

A useful method to study liquid crystalline chirality induced by chiral colloids is to observe the curvature of domain walls between right and left-handed twist domains in a 90° nematic twist cell. Using the very sensitive method of Raynes (Ref. 78, see Figure 28), our mixture was found to exhibit an average mechanical twist over macroscopic (millimeter) length scales [79]. We determined the nanotube-induced chiral pitch length P as a function of the average nanotube concentration by measuring the radii of curvature of reverse twist disclination lines in 90° nematic twist cells. The results suggest that the nanotubes' spatial concentration can vary significantly across the face of the cell, and that at high average concentrations (wt.-fraction > 0.002) the nanotubes undergo aggregation, resulting in an apparent saturation of P^{-1}. We also have been able to determine the macroscopic helical twisting power of the nanotubes.

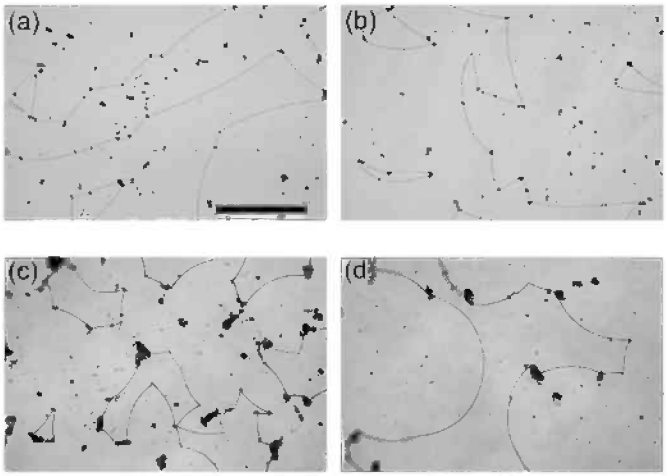


Fig. 28 Micrographs of a 90° twist cell showing bowed disclinations of 5CB+MWCNT samples for four different average CNT concentrations C_w: (a) 0.0001, (b) 0.008, (c) 0.002, and (d) 0.003 weight fraction. The bar in (a) represents 250 μm

Publications Supported by DoE (2001-2013)

- "Nematic Liquid Crystal Polarization Gratings By Modification Of Surface Alignment," Bing Wen, R.G. Petschek, and C. Rosenblatt, **Applied Optics OT** *41*, 1246 (2002)
- "Disruption of surface-induced smectic order by periodic surface corrugations," Ghanshyam P. Sinha, Charles Rosenblatt, and Leonid V. Mirantsev, **Phys. Rev.** E *65*, 041718 (2002)
- "Depression of the Nematic - Isotropic Phase Transition Temperature at nanopatterned surfaces," Bing Wen, J.-H. Kim, H. Yokoyama, and C. Rosenblatt, **Phys. Rev. E** *66*, 041502 (2002)
- "First order Fréedericksz transition above the nematic – smectic A phase transition," Wen Bing and C. Rosenblatt, **Phys. Rev. Lett.** *89*, 195505 (2002)
- "Continuous nematic anchoring transition due to surface-induced smectic order," T. Shioda, Bing Wen, and Charles Rosenblatt, **Phys. Rev. E** *67*, 041706 (2003).
- "Transverse surface-induced polarization at a chiral nematic - substrate interface," I.M. Syed and C. Rosenblatt, **Phys. Rev. E** *67*, 041707 (2003)
- "Surface-induced molecular tilt above the smectic-A – smectic-C phase transition in a nonchiral liquid crystal," I.M. Syed and C. Rosenblatt, **Phys. Rev. E** *68*, 031701 (2003)
- "Step-wise Fréedericksz transition in a nematic liquid crystal," T. Shioda, Bing Wen, and C. Rosenblatt, **J. Appl. Phys.** *94*, 7502 (2003).
- "Nanostructured Surfaces: Scientific And Optical Device Applications," C. Rosenblatt, **Mol. Cryst. Liq. Cryst**. *412*, 117 (2004)
- "Large polar pretilt for the liquid crystal homologous series alkylcyanobiphenyl," Z. Huang and C. Rosenblatt, **Appl. Phys. Lett.** 86, 011908 (2005)
- "Polar anchoring strength of a tilted nematic: Confirmation of the dual easy axis model," G. Carbone and C. Rosenblatt, **Phys. Rev. Lett.** 94, 057802 (2005)
- "Planar degenerate substrate for micro- and nanopatterned nematic liquid crystals," I.M. Syed, G. Carbone, C. Rosenblatt, and B. Wen, **J. Appl. Phys.** *98*, 034303 (2005).
- "Smectic tilt susceptibility: Anharmonic behavior in surface-induced smectic layers above the nematic -- smectic-A transition temperature," Z. Huang, G. Carbone, C. Xia, G.P. Sinha, and C. Rosenblatt, **Phys. Rev. E.** *72*, 021708 (2005)
- "Quasi-divergent nematic surface electroclinic coefficient," M.H. Zhu, G. Carbone, and C. Rosenblatt, **Phys. Rev. E** *73*, 041701 (2006)
- "Electrically-switchable, polarization-independent diffraction grating based on negative dielectric anisotropy liquid crystal," Min Hua Zhu, G. Carbone, and Rosenblatt **Appl. Phys. Lett.** *88*, 253502 (2006)
- "Rubbing-induced anisotropy of long alkyl side chains at polyimide surfaces," H.D. Jayathilake, M.H. Zhu, C. Rosenblatt, A.N. Bordenyuk, C. Weeraman, and A.V. Benderskii, **J. Chem. Phys.** *125*, 064706 (2006)
- "Bend expulsion from the smectic-A phase: Analogy to type-I superconductor," R. Wang, I.M. Syed, G. Carbone, R.G. Petschek, and C. Rosenblatt, **Phys. Rev. Lett.** *97*, 167802 (2006)

- "Continuous control of liquid crystal pretilt angle from homeotropic to planar," K. Vaughn, M. Sousa, D. Kang, and C. Rosenblatt, **Appl. Phys. Lett.** *90*, 194102 (2007)
- "Optical Nanotomography of anisotropic fluids," Antonio De Luca, Valentin Barna, T.J. Atherton, G.i Carbone, M.E. Sousa, and C. Rosenblatt, **Nature Physics** *4*, 869 (2008)
- "Nanoscale anisotropic patterning for alignment of a birefringent fluid and nanoimaging of its optical phase retardation," V. Barna, A. De Luca, and C. Rosenblatt, **Nanotechnology** *19*, 325709 (2008)
- "Diverging Elasticity and Director Uniformation in a Nanopatterned Cell near the Nematic - Smectic-A Phase Transition," T.J. Atherton, R. Wang, and C. Rosenblatt, **Phys. Rev. E** *77*, 061702 (2008)
- "Patterning-induced surface chirality and modulation of director twist in a nematic cell", Yoonseuk Choi, Timothy Atherton, Sameh Ferjani, Rolfe G. Petschek, and Charles Rosenblatt, **Phys. Rev. E** *80*, 060701(R) (2009)
- "Direct measurement of surface-induced orientational order parameter profile above the nematic -- isotropic phase transition temperature," Ji-Hoon Lee, Timothy J. Atherton, Valentin Barna, Antonio De Luca, Emanuela Bruno, Rolfe G. Petschek, and Charles Rosenblatt, **Phys. Rev. Lett.** *102*, 167801 (2009)
- "Surface chirality-induced modulation of director twist in a nematic cell," Y. Choi, T.J. Atherton, and C. Rosenblatt, **Phys. Rev. E** *80*, 060701 (2009)
- "Full control of nematic pretilt angle using spatially homogeneous mixtures of two polyimide alignment materials," J.-H. Lee, D. Kang, C.M. Clarke, and C. Rosenblatt, **J. Appl. Phys.** *105*, 023508 (2009)
- "Direct measurement of surface-induced orientational order parameter profile above the nematic -- isotropic phase transition temperature," Ji-Hoon Lee, Timothy J. Atherton, Rolfe G. Petschek, and Charles Rosenblatt, **Phys. Rev. Lett.** 102, 167801 (2009)
- "Mechanically generated surface chirality at the nanoscale," S. Ferjani, Y. Choi, J. Pendery, R.G. Petschek, and C. Rosenblatt, **Phys. Rev. Lett.** *104*, 257801 (2010)
- "Direct visualization and measurement of the extrapolation length on cooling toward the nematic — smectic-A phase transition temperature," Yoonseuk Choi and Charles Rosenblatt, **Phys. Rev. E** *81*, 051708 (2010)
- "Carbon nanotube-induced chirality in an achiral liquid crystal," Rajratan Basu, Krysta A. Boccuzzi, Sameh Ferjani, and Charles Rosenblatt," **Appl. Phys. Lett.** *97*, 121908 (2010)
- "Mechanically generated surface chirality: Control of chiral strength," Sameh Ferjani, Joel Pendery, and Charles Rosenblatt, **Appl. Phys. Lett.** *97*, 121905 (2010)
- "Carbon nanotube-induced macroscopic helical twist in an achiral nematic liquid crystal," Rajratan Basu, Chia-Ling Chen, and Charles Rosenblatt, **J. Appl. Phys.** *109*, 083518 (2011)
- "Nematic electroclinic effect in a carbon nanotube-doped achiral liquid crystal," Rajratan Basu, Rolfe G. Petschek, and Charles Rosenblatt, **Phys Rev. E** *83*, 041707 (2011)
- "Spatially controllable surface chirality at the nanoscale," J. Pendery, S. Ferjani, C. Rosenblatt, and R.G. Petschek, **Europhys. Lett**. *96*, 26001 (2011)

- "Macroscopic torsional strain and induced molecular conformational chirality," R. Basu, J. Pendery, R.G. Petschek, R.P. Lemieux, and C. Rosenblatt, **Phys. Rev. Lett.** *107*, 237804 (2011)
- "Chiral induction in thioester and oxoester liquid crystals by dispersed carbon nanotubes," Rajratan Basu, Charles Rosenblatt, and Robert P. Lemieux, **Liq. Cryst.** *39*, 199 (2012)
- "Probing the Pore Structure of a Chiral Periodic Mesoporous Organosilica Using Liquid Crystals," Vallamkondu Jayalakshmi, Thomas Wood, Rajratan Basu, Jenny Du, Thomas Blackburn, Charles Rosenblatt, Cathleen M. Crudden, and Robert P. Lemieux, **J. Mater. Chem.** *22*, 15255 (2012)
- "Nematic Twist Cell: Strong Chirality Induced at the Surfaces," Tzu-Chieh Lin, Ian R. Nemitz, Joel S. Pendery, Christopher P.J. Schubert, Robert P. Lemieux, and Charles Rosenblatt, **Appl. Phys. Lett.** *102,* 134101 (2013)
- "Nematic molecular core flexibility and chiral induction",Tzu-Chieh Lin, Ian R. Nemitz, Christopher J. McGrath, Christopher P. J. Schubert, Hiroshi Yokoyama, Robert P. Lemieux, and Charles Rosenblatt, **Phys. Rev. E** *88*, 042501 (2013)
- "Optical imaging of liquid crystals at the nanoscale," C. Rosenblatt, **ChemPhysChem** (In press) [Galley proofs appended]

References

1. J. Cognard, "Alignment of nematic liquid crystals and their mixtures," Mol. Cryst. Liq. Cryst. Suppl. 1, 1 (1982)

2 D.W. Berreman, "Solid surface shape and alignment of an adjacent nematic liquid crystal," Phys. Rev. Lett. **28**, 1683 (1972)

3 J.M. Geary, J.W. Goodby, A. Kmetz, and J.S. Patel, "The mechanism of polymer alignment of liquid-crystal materials," J. Appl. Phys. **62**, 4100 (1987)

4. "Surface-induced parallel alignment of liquid-crystals by linearly polymerized photopolymers," M. Schadt, K. Schmidt, V. Kozenkov, and V. Chigrinov, Jpn. J. Appl. Phys. **31**, 2155 (1992)

5. "Photosensitive Orientants for Liquid Crystal Alignment," T. Marusii and Y. Reznikov, Mol. Mater. **3**, 161 (1993)

6. "Alignment control of liquid crystal molecules using photo-dimerization reaction of poly(vinyl cinnamate)," Y. Iimura, S. Kobayashi, T. Hashimoto, T. Sugiyama, and K. Katoh, IEICE Trans. Electron. **E79-C**, 1040 (1996)

7. "Investigation Of Liquid-Crystal Alignment On Polybutylmethacrylate Surfaces Using Ftir-ATR and XPS," E.A. Thomas, T.A. Zupp, J.E. Fulghum, D.S. Fredley, and J.L. West, Mol. Cryst. Liq. Cryst. **250**, 193 (1994)

8. "Atomic-beam alignment of inorganic materials for liquid-crystal displays," P. Chaudhari, *et al.*, Nature, **411**, 56 (2001)

9 J. Cognard, "Alignment of nematic liquid crystals and their mixtures," Mol. Cryst. Liq. Cryst. Suppl. 1, 1 (1982)

10 G.P. Sinha, B. Wen, and C. Rosenblatt, "Large, continuously controllable nematic pretilt from vertical orientation," Appl. Phys. Lett. **79**, 2543 (2001)

11 "Continuous nematic anchoring transition due to surface-induced smectic order," T. Shioda, Bing Wen, and Charles Rosenblatt, Phys. Rev. E *67*, 041706 (2003).

12. A. Rapini and M. Papoular, "Distorsion D'une Lamelle Nematique Sous Champ Magnetique Conditions D'ancrage aux Parois," J. Physique Colloq. **30**, C4-54 (1969)

13 "Polar anchoring strength of a tilted nematic: Confirmation of the dual easy axis model," G. Carbone and C. Rosenblatt, Phys. Rev. Lett. 94, 057802 (2005)

14. "Large polar pretilt for the liquid crystal homologous series alkylcyanobiphenyl," Z. Huang and C. Rosenblatt, Appl. Phys. Lett. (in press)

15. W. Chen, L.J. Martinez-Miranda, H. Hsiung, and Y.R. Shen, "Orientational Wetting Behavior Of A Liquid-Crystal Homologous Series," Phys. Rev. Lett. **62**, 1860 (1989)

16 "Surface-induced molecular tilt above the smectic-A – smectic-C phase transition in a nonchiral liquid crystal," I.M. Syed and C. Rosenblatt, Phys. Rev. E *68*, 031701 (2003)

17. "Transverse surface-induced polarization at a chiral nematic - substrate interface," I.M. Syed and C. Rosenblatt, Phys. Rev. E *67*, 041707 (2003)

18. R.B. Meyer, L. Liebert, L. Strzelecki, and P. Keller, "Ferroelectric liquid crystals," J. Phys. (France) Lett. **36**, L69 (1975)

19. J. Shi, "Criteria for the first order Fréedericksz transition," Liq. Cryst. **29**, 121 (2002)

20. K.H. Yang and C. Rosenblatt, "Determination of the anisotropic potential at the nematic liquid crystal-to-wall interface," Appl. Phys. Lett. **43**, 62 (1983)

21. "First order Fréedericksz transition above the nematic – smectic A phase transition," Wen Bing and C. Rosenblatt, Phys. Rev. Lett. *89*, 195505 (2002)
22 Bing Wen, M.P. Mahajan, and C. Rosenblatt, "Ultrahigh resolution liquid crystal display with gray scale," Appl. Phys. Lett. **76**, 1240 (2000)
23. C. Rosenblatt, "Liquid crystal Fréedericksz transition and surface-induced smectic ordering," Phys. Rev. Lett. **53**, 791 (1984).
24 "Disruption of surface-induced smectic order by periodic surface corrugations," Ghanshyam P. Sinha, Charles Rosenblatt, and Leonid V. Mirantsev, Phys. Rev. E *65*, 041718 (2002)
25. L.V. Mirantsev, "Deformed surface-induced smectic A structure in a nematic liquid crystal," Mol. Cryst. Liq. Cryst. **301**, 137 (1997).
26. G. Barbero and G. Durand, "Curvature induced quasi-melting from rough surfaces in nematic liquid crystals," J. Physique II **1**, 651 (1991)
27. M. Monkade, P. Martinot-Lagarde, G. Durand, and G. Granjean, "SiO evaporated films topography and nematic liquid crystal orientation," J. Physique II **7**, 1577 (1997)
28. J. Papanek and P. Martinot-Lagarde, "Nematic order melting on rough surfaces measured by surface plasmon resonance," J. Physique II **6**, 205 (1996)
29. "Depression of the Nematic - Isotropic Phase Transition Temperature at nanopatterned surfaces," Bing Wen, J.-H. Kim, H. Yokoyama, and C. Rosenblatt, Phys. Rev. E *66*, 041502 (2002)
30 "Depression of the Nematic - Isotropic Phase Transition Temperature at nanopatterned surfaces," Bing Wen, J.-H. Kim, H. Yokoyama, and C. Rosenblatt, Phys. Rev. E *66*, 041502 (2002)
31. "Step-wise Fréedericksz transition in a nematic liquid crystal," T. Shioda, Bing Wen, and C. Rosenblatt, J. Appl. Phys. *94*, 7502 (2003).
32 "Step-wise Fréedericksz transition in a nematic liquid crystal," T. Shioda, Bing Wen, and C. Rosenblatt, J. Appl. Phys. *94*, 7502 (2003).
33. "Nematic Liquid Crystal Polarization Gratings By Modification Of Surface Alignment," Wen Bing, R.G. Petschek, and C. Rosenblatt, Applied Optics OT *41*, 1246 (2002)
34 "Smectic tilt susceptibility: Anharmonic behavior in surface-induced smectic layers above the nematic -- smectic-A transition temperature," Z. Huang, G. Carbone, C. Xia, G.P. Sinha, and C. Rosenblatt, Phys. Rev. E. *72*, 021708 (2005)
35 G.P. Sinha, B. Wen, and C. Rosenblatt, "Large, continuously controllable nematic pretilt from vertical orientation," Appl. Phys. Lett. 79, 2543 (2001)
36. "Continuous nematic anchoring transition due to surface-induced smectic order," T. Shioda, Bing Wen, and Charles Rosenblatt, Phys. Rev. E *67*, 041706 (2003).
37. "Quasi-divergent nematic surface electroclinic coefficient," M.H. Zhu, G. Carbone, and C. Rosenblatt, Phys. Rev. E *73*, 041701 (2006)
38 "Quasi-divergent nematic surface electroclinic coefficient," M.H. Zhu, G. Carbone, and C. Rosenblatt, Phys. Rev. E *73*, 041701 (2006)
39. "Planar degenerate substrate for micro- and nanopatterned nematic liquid crystals," I.M. Syed, G. Carbone, C. Rosenblatt, and B. Wen, J. Appl. Phys. *98*, 034303 (2005).
40. "Rubbing-induced anisotropy of long alkyl side chains at polyimide surfaces," H.D. Jayathilake, M.H. Zhu, C. Rosenblatt, A.N. Bordenyuk, C. Weeraman, and A.V. Benderskii, J. Chem. Phys. *125*, 064706 (2006)

41 K.E. Vaughn, M. Sousa, D. Kang, and C. Rosenblatt, "Continuous control of liquid crystal pretilt angle from homeotropic to planar," Appl. Phys. Lett. 90, 194102 (2007)
42 J.T.K. Wan, O.K.C. Tsui, H.S. Kwok, and P. Sheng, "Liquid crystal pretilt control by inhomogeneous surfaces" Phys. Rev. E 72, 021711 (2005)
43. "Full control of nematic pretilt angle using spatially homogeneous mixtures of two polyimide alignment materials," J.-H. Lee, D. Kang, C.M. Clarke, and C. Rosenblatt, J. Appl. Phys. *105*, 023508 (2009)
44. B. Wen, R.G. Petschek, and C. Rosenblatt, "Nematic liquid crystal polarization gratings by modification of surface alignment," Appl. Opt. 41, 1246 (2002)
45. B. Wen, M.P. Mahajan, C. Rosenblatt, "Ultrahigh resolution liquid crystal display with gray scale," Appl. Phys. Lett. 76, 1240 (2000)
46. "Electrically-switchable, polarization-independent diffraction grating based on negative dielectric anisotropy liquid crystal," Min Hua Zhu, G. Carbone, and Rosenblatt Appl. Phys. Lett. *88*, 253502 (2006)
47. P.G. DeGennes, "An analogy between superconductors and smectics A," Sol. State Comm. 10, 753 (1972)
48. "Bend expulsion from the smectic-A phase: Analogy to type-I superconductor," R. Wang, I.M. Syed, G. Carbone, R.G. Petschek, and C. Rosenblatt, Phys. Rev. Lett. *97*, 167802 (2006)
49 J.T.K. Wan, O.K.C. Tsui, H.S. Kwok, and P. Sheng, "Liquid crystal pretilt control by inhomogeneous surfaces" Phys. Rev. E 72, 021711 (2005)
50 P.G. DeGennes, "An analogy between superconductors and smectics A," Sol. State Comm. 10, 753 (1972)
51. "Diverging Elasticity and Director Uniformation in a Nanopatterned Cell near the Nematic - Smectic-A Phase Transition," T.J. Atherton, R. Wang, and C. Rosenblatt, Phys. Rev. E *77*, 061702 (2008)
52. "Optical Nanotomography of anisotropic fluids," Antonio De Luca, Valentin Barna, Timothy J. Atherton, Giovanni Carbone, Matthew E. Sousa, and Charles Rosenblatt, Nature Physics *4*, 869 (2008)
53. "Nanoscale anisotropic patterning for alignment of a birefringent fluid and nanoimaging of its optical phase retardation," V. Barna, A. De Luca, and C. Rosenblatt, Nanotechnology *19*, 325709 (2008)
54. "Boundary layer phase transition in nematic liquid crystals," Ping Sheng, Phys. Rev. A 26, 1610 (1982)
55. T.J. Sluckin and A. Poniewierski, "The theory of the nematic-isotropic transition in a restricted geometry," Liq. Cryst. 2, 281 (1987)
56. H. Yokoyama, S. Kobayashi, and H. Kamei, "Boundary dependence of the formation of new phase at the isotropic-nematic transition," Mol. Cryst. Liq. Cryst. 99, 39 (1983)
57. K. Kocevar, A. Borstnik, I Musevic, and S. Zumer, "Capillary Condensation of a Nematic Liquid Crystal Observed by Force Spectroscopy," Phys. Rev. Lett. 86, 5914 (2001)
58. "Direct measurement of surface-induced orientational order parameter profile above the nematic -- isotropic phase transition temperature," Ji-Hoon Lee, Timothy J. Atherton, Rolfe G. Petschek, and Charles Rosenblatt, Phys. Rev. Lett. (submitted)
59 "Surface induced weak orientational order and role of isotropic-nematic interface fluctuations in the appearance of an induced nematic phase," Elena S. Pikina and Charles Rosenblatt, **Eur. Phys. J. E** *35*, 87 (2012)

60 Yoonseuk Choi and Charles Rosenblatt, "Direct visualization and measurement of the extrapolation length on cooling toward the nematic — smectic-A phase transition temperature," Phys. Rev. E **81**, 051708 (2010)
61 D. Davidov, C. R. Safinya, M. Kaplan, S. S. Dana, R. Schaetzing, R. J. Birgeneau, and J. D. Litster, "High-resolution x-ray and light-scattering study of critical behavior associated with the nematic—smectic-*A* transition in 4-cyano-4′-octylbiphenyl, Phys. Rev. B **19**, 1657 (1979)
62 "Patterning-induced surface chirality and modulation of director twist in a nematic cell", Yoonseuk Choi, Timothy Atherton, Sameh Ferjani, Rolfe G. Petschek, and Charles Rosenblatt, **Phys. Rev. E** *80*, 060701(R) (2009)
63 "Mechanically generated surface chirality at the nanoscale," S. Ferjani, Y. Choi, J. Pendery, R.G. Petschek, and C. Rosenblatt, **Phys. Rev. Lett.** *104*, 257801 (2010)
64 "Mechanically generated surface chirality: Control of chiral strength," Sameh Ferjani, Joel Pendery, and Charles Rosenblatt, **Appl. Phys. Lett.** *97*, 121905 (2010)
65 "Spatially controllable surface chirality at the nanoscale,"J. Pendery, S. Ferjani, C. Rosenblatt, and R.G. Petschek, **Europhys. Lett**. *96*, 26001 (2011)
66 "Macroscopic torsional strain and induced molecular conformational chirality," R. Basu, J. Pendery, R.G. Petschek, R.P. Lemieux, and C. Rosenblatt, **Phys. Rev. Lett.** *107*, 237804 (2011)
67 "Nematic Twist Cell: Strong Chirality Induced at the Surfaces," Tzu-Chieh Lin, Ian R. Nemitz, Joel S. Pendery, Christopher P.J. Schubert, Robert P. Lemieux, and Charles Rosenblatt, **Appl. Phys. Lett.** *102,* 134101 (2013)
68 See this and the following two review: "Syntheses, properties and applications of periodic mesoporous organosilicas prepared from bridged organosilane precursors", N. Mizoshita, T. Tani, and S. Inagaki, Chem. Soc. Rev. **40**, 789 (2011)
69 Q. Yang, J. Liu, L. Zhang, and C. Li, "Functionalized periodic mesoporous organosilicas for catalysis", J. Mat. Chem. **19**, 1945 (2009)
70 W.J. Hunks and G.A. Ozin, "Challenges and advances in the chemistry of periodic mesoporous organosilicas (PMOs)", J. Mat. Chem. **15**, 3716 (2005)
71 T.Y. Zhuang, J.Y. Shi, B.C. Ma, and W. Wang, "Chiral norbornane-bridged periodic mesoporous organosilicas", J. Mat. Chem. **20**, 6026 (2010)
72 P. Wang, J. Yang, J. Liu, L. Zhang, and Q. Yang, "Chiral mesoporous organosilicas with R-(+)-Binol integrated in the framework", Microporous Mesoporous Mat. **117**, 91 (2009)
73 "Probing the Pore Structure of a Chiral Periodic Mesoporous Organosilica Using Liquid Crystals," Vallamkondu Jayalakshmi, Thomas Wood, Rajratan Basu, Jenny Du, Thomas Blackburn, Charles Rosenblatt, Cathleen M. Crudden, and Robert P. Lemieux, **J. Mater. Chem.** *22*, 15255 (2012)
74 "Carbon nanotube-induced chirality in an achiral liquid crystal," Rajratan Basu, Krysta A. Boccuzzi, Sameh Ferjani, and Charles Rosenblatt," **Appl. Phys. Lett.** *97*, 121908 (2010)
75 "Chiral induction in thioester and oxoester liquid crystals by dispersed carbon nanotubes," Rajratan Basu, Charles Rosenblatt, and Robert P. Lemieux, **Liq. Cryst.** *39*, 199 (2012)
76 "Nematic electroclinic effect in a carbon nanotube-doped achiral liquid crystal," Rajratan Basu, Rolfe G. Petschek, and Charles Rosenblatt, **Phys Rev. E** *83*, 041707 (2011)
77 R. Berardi, H.-G. Kuball, R. Memmer, and C. Zannoni, "Chiral induction in nematics: a computer simulation study", J. Chem. Soc., Faraday Trans., **94**, 1229 (1998).
78 E.P. Raynes, "The use of bowed reverse twist disclination lines for the measurement of long pitch lengths in chiral nematic liquid crystals", Liq. Cryst. 33, 1215 (2006)

79 “Carbon nanotube-induced macroscopic helical twist in an achiral nematic liquid crystal,” Rajratan Basu, Chia-Ling Chen, and Charles Rosenblatt, **J. Appl. Phys.** *109*, 083518 (2011)

ChemPubSoc Europe

DOI: 10.1002/cphc.201300978

Optical Imaging of Liquid Crystals at the Nanoscale

Charles Rosenblatt*[a]

The instrumentation associated with near-field scanning optical microscopy (NSOM) can be exploited to provide three-dimensional structure and dynamic information about liquid crystals at scales not possible with diffraction-limited tools. This Minireview focuses on our use of NSOM techniques to probe spatial variations of the nematic director and the nematic orientational order parameter on length scales as small as a few nanometers.

1. Introduction

One of the hallmarks of liquid crystals is their large optical birefringence,[1] which provides a plethora of scientific phenomena and applications.[2] The liquid crystal director can be coupled to, and manipulated externally by, electric, magnetic, optical, and flow fields, as well as by temperature and by anisotropic van der Waals interactions at an interface. The resulting modification of the nematic tensorial order parameter can be observed as a change in the optical properties of the liquid crystal.[1] The experimentalist's toolkit contains a variety of optical techniques, beginning with polarized optical microscopy, by which a myriad of beautiful images of liquid crystal textures have been obtained.[3] Confocal microscopy[4–6] is used to obtain three dimensional (3D) images of liquid crystalline order, as well as of mixtures of liquid crystals and colloids. Laser-based birefringence studies provide key information about field-induced switching of the director, that is, the Freedericksz transition;[1,2] the orientational order induced by a substrate;[7–9] and pre-transitional phenomena.[10] Measurements of circular dichroism allow the researcher to investigate chiral properties.[11–13] Light scattering in the visible part of the spectrum facilitates studies of order parameter fluctuations, that is, broken symmetry modes,[14–17] as well as static structural properties.[18] But the element that is common to all of these optical approaches is diffraction: Features smaller than a few hundred nanometers cannot be imaged easily with visible light. In some cases one can exploit prior knowledge about the system, such as the structure of a suspended colloid, along with an appropriate model, such as Mie scattering, to back out information about the combined liquid crystal/colloid system on very short length scales.[19] Alternatively, 3D nonlinear microscopic techniques can improve slightly on the diffraction limit,[20,21] as can 3D holographic manipulation (i.e. tweezers) of specific colloids inside the liquid crystal.[22] However, model-free imaging at length scales well below a few hundred nanometers cannot be accomplished with this optical kit, at least in the visible part of the spectrum.

About eighty years ago Synge suggested[23] that the diffraction limit could be circumvented by using an aperture of dimensions much smaller than the wavelength of light. To mitigate losses associated with the evanescent components of light, he suggested that the aperture be placed very close to the sample's surface, thus facilitating an optical measurement that corresponds to a very small region of the sample.[23] With the advent of scanning tunneling microscopy in the early 1980s,[24] new methods of scanning probe microscopies were developed, including near-field scanning optical microscopy (NSOM), which facilitates sub-wavelength of light optical resolution.[25–28] In its simplest and original form, NSOM involves an optical fiber with an ultra-small aperture, typically 50–100 nm in diameter. The fiber is brought within a few nanometers of the surface to be imaged and scanned (by means of piezoelectrics) in the *xy* plane at this fixed height above the surface. Height control often involves mounting a fiber onto a tuning fork that is driven electrically by a piezoelectric mounted to the fork. As the height of the fiber is varied, the interaction between the fiber and surface changes, resulting in changes of the phase and amplitude of the tuning fork vibrations. The electrical signal from a piezoelectric mounted to the tuning fork is then fed into a feedback loop to maintain a fixed height of the fiber above the surface. The fiber can serve as the light source that illuminates a very small area, with collection optics and detector either for reflected light or for transmitted light downstream. Alternatively, the sample can be illuminated over a wide area, and the fiber can be used to collect light from a very small, sub-wavelength light region of the sample. Since the computer "knows" the *x,y,* and *z* coordinates of the aperture, an intensity-versus-position map can be created, with lateral resolution as small as several tens of nanometers. There are many variations to this scenario, including apertureless probes, atomic force microscopy (AFM)/NSOM hybrid probes■■ok?■■, the use of polarized light, time-sensitive measurements of transient phenomena, *z*-dependent detection, and immersion of the fiber into a (soft) sample.

It was not until the early to mid-1990s that NSOM techniques were applied to liquid crystals. This is perhaps a bit sur-

[a] *Prof. C. Rosenblatt*
Department of Physics
Case Western Reserve University
Cleveland, Ohio 44106 (USA)
Fax: (+1) 216-368-4671
E-mail: rosenblatt@case.edu

WILEY-VCH Galley Proof

prising, given the rapid maturation of the experimental technique and the extraordinary level of liquid crystal research activity in the late 1980s and early 1990s, with the great advances in liquid crystal display technology.[2] Even to this day there are a multitude of outstanding scientific problems that need to be addressed using NSOM and its offshoots. In this Minireview I first present some of the important results to date, and then turn to some of the results that emanate from my own laboratory, which focuses on *z*-dependent imaging inside the liquid crystal.

2. NSOM and Liquid Crystals

One of the earliest published works on NSOM studies of liquid crystals appeared in 1995. Here Moyer, et al. used reflection imaging in shear-force mode above a smectic-A liquid crystal/air interface to measure simultaneously the polarized reflected light and the topography of the interface.[29] Although they observed a smooth topography, their optical signal clearly showed NSOM probe-induced features that were uncorrelated with the topographical image, including a reorientation of the liquid crystal director. The authors conjectured that this may have been caused by heating due to optical loss near the end of the probe, by the optical field emanating from the aperture, or perhaps by a capillary surface surrounding the probe that probably was immersed a small distance (perhaps ~5 nm) into the liquid crystal. Most importantly, however, they made an initial foray into *z*-dependent measurements, showing that once the fiber reaches the liquid crystal/air interface, it can be submerged controllably along the *z*-axis all the way to the substrate, which they presciently noted is "potentially very useful for 3D (NSOM) investigations of this and other liquid samples."[29]

Shortly thereafter Williamson and Miles performed a shear-force measurement inside a thin layer of octylcyanobiphenyl liquid crystal in the smectic-A phase,[30] demonstrating how the amplitude of the probe oscillations reflects the smectic layer structure. This was a purely mechanical measurement and a precursor to the more precise mechanical AFM measurements on smectic layering by Kočevar and Muševič.[31] Williamson and Miles, however, limited their optical imaging to the fiber hovering above the liquid crystal/air surface.

During the late 1990s and early 2000s most of the NSOM-based work on liquid crystals involved imaging from just outside a thin liquid crystal film. Ade, et al., used optically polarized light to examine the structure of polymer-dispersed liquid crystal composites in light of theoretical models for these samples.[32] Similarly, Ramanujam, et al. imaged a polarization holographic grating in an azobenzene side chain liquid crystalline polyester,[33] showing that the film remains optically anisotropic after >20 h, despite the disappearance of the grating structure—as measured by AFM—over this period of time. Huser, et al., turned their attention to cholesteric liquid crystal films, obtaining images of the classical fingerprint textures and obtaining quantitative birefringence data using a Mueller–Stokes formalism, which is normally valid in the far-field limit.[34] In fact, far-field optics can be used to analyze data from a variety of NSOM-based birefringence-type experiments, as we see later. In 2006 Bechtold, et al used NSOM to examine the liquid crystal orientation above nanopatterned surfaces, again maintaining the probe just outside the liquid crystal film,[35] and Lukishova and Schmid studied two dimensional hexagonal structures in the defects of cholesteric oligomeric liquid crystal films.[36]

In 1998 Mei and Higgins pioneered dynamic NSOM studies of liquid crystalline materials.[37] Exploiting the aluminum cladding of their NSOM probes, they applied a large electric field between the end of the probe (surrounding the aperture) and a semi-transparent, electrically conducting indium-tin-oxide coated glass slide, which served as support for a thin film of polymer-dispersed liquid crystal. On applying a sinusoidally modulated voltage from the air/film surface, they were able to observe time-dependent intensity variations using polarized light and phase-locked electrooptic techniques, thus providing information about switching dynamics. The applied electric field strength was greatest close to the end of the probe, which corresponds to the near-field optical region. But given that the film thickness was ~1 μm, much of the probed volume resided in the far optical field, where the applied electric field was weak. Thus, the region in which the switching dynamics were probed by the NSOM depended on both the region in which the switching was induced and on the near- and far-field regions traversed by the light. In subsequent work they demonstrated that it is possible to confine the switching to regions probed only in the near-field optical regime.[38] In the end, they were able to probe the dynamics in volumes as small as 10^{-15} cm^3. Mei and Higgins continued this applied electric field approach to study dynamics in polymer-dispersed liquid crystal films. These include a study of electric field-induced ion migration dynamics in which a film was doped with a salt, resulting in a charged double layer at the polymer/liquid crystal interface and a decrease in the liquid crystal relaxation time,[39] and an investigation of the dynamics of a dye-doped polymer-dispersed liquid crystal.[40] Hall and Higgins went on to perform a study of photorefractive effects in dye-doped materials in which they obtained information about photogeneration of ions, their migration, and their effect on liquid crystal orientation.[41] A review of this work can be found in ref. [42].

Combining the concepts of probe immersion inside the liquid crystal and electric field application between the metal-clad probe and a semi-transparent conducting substrate, Tadokoro, et al. demonstrated depth profiling of liquid crystal order and electrically induced switching, as well as 2D imaging of liquid crystal orientational order in the presence of an electric field.[43] They immersed an NSOM fiber into a liquid crystal film, controlling the distance between the probe and substrate using an infrared evanescent-field feedback system (rather than a vibrating tuning fork) in conjunction with a second detector that senses the feedback light through the optical fiber. By mechanical manipulation, the authors closed off the aperture with an ultra-thin metallic film that facilitated a quasi-planar electrode at the probe's apex as well as a well-defined circular near-field light spot, the latter greatly simplifying the polarization state of the light.[44] A hallmark of this work was

© 2014 Wiley-VCH Verlag GmbH & Co. KGaA, Weinheim

the measurement of the optical intensity of the transmitted visible light from the fiber as a function of applied electric field and height z above the substrate, where $300\,nm < z < 3\,\mu m$. They found excellent qualitative and good quantitative agreement with a theoretical calculation for the intensity based on continuum elastic theory[45] and a plane-wave optics approximation. The following year they applied their apparatus to the study of in-plane electric switching (IPS) from a fixed height above the liquid crystal/air interface.[46] Taking this idea a step further, Qin, et al. examined IPS dynamics inside the liquid crystal as a function of the position z above the substrate,[47] where they obtained the field-induced switching and relaxation times through birefringence measurements.

Based on many of these advances, in the mid to late 2000s my group saw the opportunity to use NSOM technology to image quantitatively the internal order of a liquid crystal film in three dimensions—with unprecedented spatial resolution. But there were many hurdles to overcome. We first addressed the issue of optics: Can birefringence intensity data be analyzed in the relatively simple far-field approximation of a plane wave? Among the many geometries in which a near-field scanning optical microscope can be operated, we chose to use an aluminum-cladded fiber for illumination, with detection downstream, as shown schematically in Figure 1.

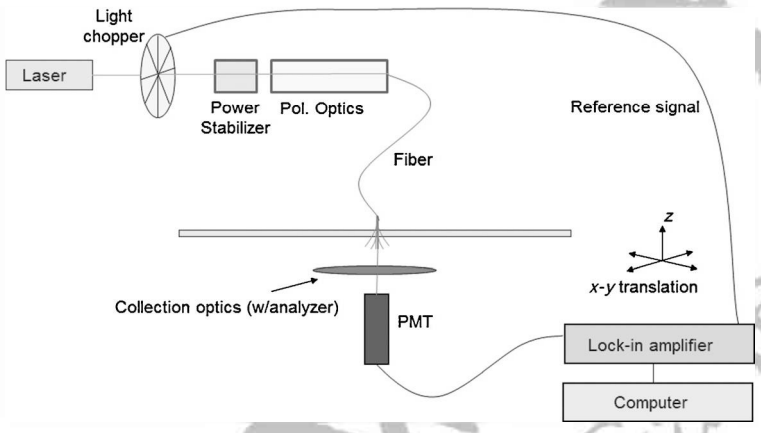


Figure 1. Representation of NSOM setup. Polarization optics includes polarizer and $\lambda/2$ and $\lambda/4$ waveplates. Collection optics include lenses and a bandpass filter at the appropriate laser wavelength.

Using nominally circularly polarized light at wavelength of $\lambda = 488$ nm and the liquid crystal hexylcyanobiphenyl, we lowered the fiber until it made contact with the substrate and then slowly backed it out, measuring the intensity at the detector as a function of z; see Figure 2. For quasi-circularly polarized light the intensity using a plane-wave approximation is expected to have a constant background plus a component that varies sinusoidally with the optical retardation $\alpha = 2\pi\Delta n z/\lambda$, where Δn is the birefringence. Figure 2 shows the raw data and a sinusoidal fit, of which we extracted a birefringence of $\Delta n = 0.16$, equal to published results.[46]

The data in Figure 2 show empirically that the far-field plane-wave approximation is appropriate for analysis of birefringence data, even out to 2 μm. Despite significant signal loss due to evanescent components of light, the downstream collection optics limits the light to a sufficiently narrow cone with sufficient intensity at the detector. ■■ok?■■Moreover, at least on these length scales, the vibration of the fiber (due to the tuning fork's feedback mechanism) appears to have, at most, minimal deleterious effects on the liquid crystal orientation.

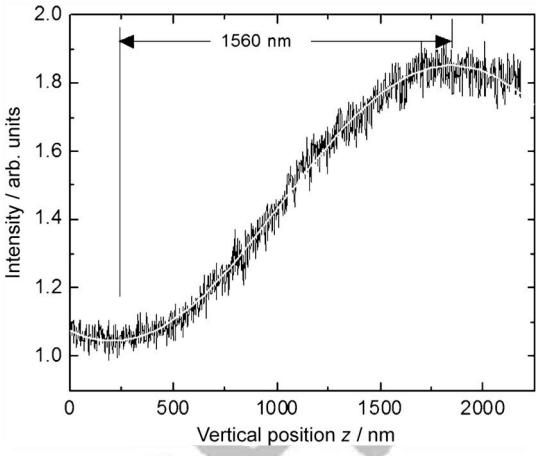


Figure 2. Intensity versus height z of fiber aperture above the substrate in liquid crystal 6CB. Solid line is a sinusoidal fit of the data.

Qin and Umeda,[49] and Qin, et al.,[50] used the oscillations of their fiber to reorient mechanically the liquid crystal. In their experiments they drove the oscillations at 1250 Hz with an amplitude of 200 nm. In our case, which is typical of standard NSOM operation, the oscillations were driven at ~100 kHz with an amplitude of a few nanometers. Given that the diameter of the probe (fiber + cladding) is ~200 nm, we can estimate the response time τ of the liquid crystal beneath the fiber as $\tau = \eta d^2/K$, where η is a viscosity ~0.1 poise [1] and $K \sim 10^{-6}$ dyn is a typical elastic constant.[1] For d we used 200 nm as a lower limit. Thus, the response time τ is several tens of microseconds, suggesting that the slow but large amplitude vibrations were responsible for the induced director reorientations in refs. [49,50]. In contrast, the much smaller oscillations and much higher frequencies used in our NSOM experiments tend to preclude such reorientations. Figure 3 shows two images, with Figure 3a obtained from a forward NSOM scan and Figure 3b from a reverse scan of a nematic liquid crystal, in which the substrate was patterned using an AFM as a scribing tool. The white arrows indicate the resulting alternating easy axes for liquid crystal alignment of $\pm 45°$. The two images are nearly identical, suggesting that the NSOM fiber did not modify the liquid crystal orientation. From this we conclude that one can measure the optical retardation over the distance from the fiber's aperture to the substrate, at least if the aperture is sufficiently far from the substrate.

A particularly useful application of NSOM is the study of nanoscopic static director structures. Owing to the liquid crys-

© 2014 Wiley-VCH Verlag GmbH & Co. KGaA, Weinheim

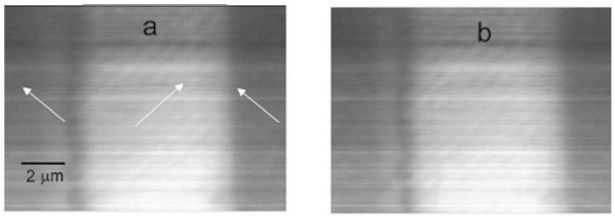


Figure 3. Forward and reverse images of a liquid crystal using crossed polarizers. The white arrows show the direction of the AFM-scribed easy axis, with AFM scribing lines spaced 50 nm apart.

tal's elasticity K, the director is unable to follow sharp changes in azimuthal orientation ϕ that are imposed by a substrate patterned for spatially varying alignment. The "extrapolation length" L corresponds to the distance over which the director is able to change orientation, and is given by $L = K/W_2$, where W_2 is the anchoring strength coefficient for deviations from the local patterned "easy axis" direction ϕ_0; that is, to lowest order the anchoring energy is $F_s = {}^1/_2 W_2(\phi - \phi_0)^2$.[1] L often is of the order of 100 to 300 nm, and until NSOM was used, had been obtained only indirectly.[51–53] Exploiting NSOM techniques, we recently made a direct visualization and measurement of L on approaching the nematic–smectic-A transition temperature T_{NA}.[54] To accomplish this, we first AFM-scribed a herringbone pattern into a polyimide, the scribed lines of which were separated by 200 nm and the herringbone period was 50 μm (Figure 4). We covered the substrate with a 5 μm

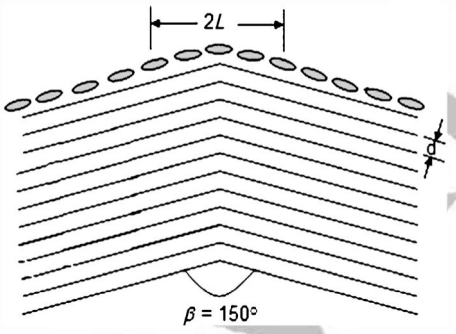


Figure 4. Representation of herringbone-shaped easy axis and molecules attempt to undergo a bend deformation around the herringbone apex.

film of the liquid crystal octylcyanobiphenyl, immersed the fiber aperture to a height of about 70 nm above the substrate, and scanned the NSOM fiber over the herringbone apex while slowly reducing the temperature.[1] The linear polarizer of the $\lambda = 532$ nm wavelength laser light and the crossed analyzer were adjusted in such a way that the intensity of the signal at the detector varied linearly with the director's local azimuthal orientation. We found that the intensity variation in the neighborhood of the apex varied more slowly in space on approaching the transition temperature T_{NA} owing to the divergence of the bend elastic constant.[55] (Figure 5)

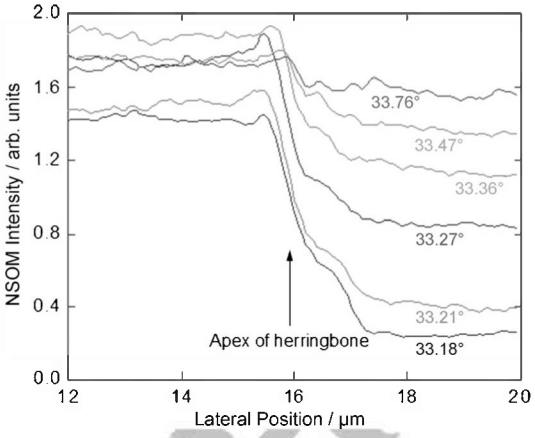


Figure 5. NSOM intensity profile at various temperatures above T_{NA} in the region where the easy axis undergoes a sharp change in direction.

The spatial extent of the intensity change does not correspond precisely to $2L$, as the results shown in Figure 5 have yet to account for the instrumental linewidth of the NSOM, consisting mostly by the partial washing out of the intensity profile due to the fiber's ~70 nm aperture diameter■■ok? wording was unclear■■. After including the instrumental characteristics, we obtained the extrapolation L versus temperature, shown in Figure 6. Here the solid line is a three-parameter fit to the data, assuming that the anchoring strength coefficient was held constant and the temperature variation was due to the divergence in the bend elasticity. The results of the fitting yielded a critical exponent $\nu_{\parallel}$ for the susceptibility, $\nu_{\parallel} = 0.65^{+0.2}_{-0.25}$, consistent with the results in ref. [55].

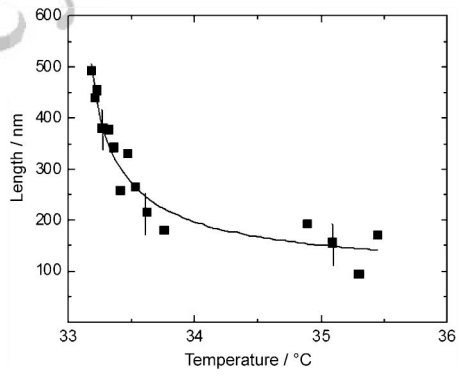


Figure 6. Extrapolation length L versus temperature. The solid line is a fit to the data assuming that the elastic modulus is a temperature-independent constant plus an algebraically divergent term.

In addition to imaging in the xy plane, NSOM can provide information about the liquid crystal director along the z axis with nanometer-scale resolution. Imaging of this sort was described in refs. [43, 46], where the vertical resolution was of the order of 100 nm, somewhat better than that obtainable from techniques such as confocal microscopy but certainly not

[1] *We controlled the temperature by lining the inside of the box containing the NSOM with red-incandescent light bulbs, thereby heating the entire apparatus uniformly. A narrow laser-line bandpass filter was placed in front of the photomultiplier detector to filter out extraneous light from the heating system.*

© 2014 Wiley-VCH Verlag GmbH & Co. KGaA, Weinheim

down to a few nanometers. Let me now turn to how NSOM can be used to examine surface-induced order.

Surface-induced orientational order above the nematic–isotropic (NI) phase transition has received extensive scrutiny.[56–62] Above the bulk first-order NI transition temperature T_{NI}, an appropriately prepared surface induces orientational order in the otherwise isotropic phase, with the order decreasing to zero as one transits into the bulk. Until recently quantitative determinations of the order parameter profile $S(z)$ versus temperature have used probes with visible-light wavelength resolution[56]—this is much larger than the length scale of the surface layer—and so required specific models in conjunction with the macroscopic data in order to extract $S(z)$.[57] Other techniques that measure local quantities, such as evanescent-wave and second-harmonic generation experiments,[8,58,59] also require specific models to extract $S(z)$.[57] We recently applied the NSOM technique to obtain a model-independent measure of surface-induced planar nematic order.[63] We measured the optical retardation α between the fiber aperture and the substrate as a function of both the aperture's height above the substrate and temperature $T > T_{NI}$. Placing a thin layer of pentylcyanobiphenyl liquid crystal on a weakly rubbed polyimide surface, we lowered the fiber until it came into contact with the substrate. While slowly backing the fiber away from the substrate, we measured the intensity of the light passing through the analyzer and into the detector as a function of height. To convert the NSOM intensity data into optical retardation, we measured the total optical retardation through a closed cell, that is, the liquid crystal sandwiched between two substrates, at the same temperatures. In the closed cell the retardation is twice that of the free surface, as orientational order develops only near the two substrates while the bulk of the closed cell remains isotropic. Figure 7 shows the retardation α versus height above the substrate at various temperatures $\Delta T = T - T_{NI}$.

Because the optical retardation is proportional to the scalar nematic order parameter S, and the proportionality constant can be determined experimentally, we were able to extract the model-independent S versus distance z from the substrate for different values of ΔT; see Figure 8.

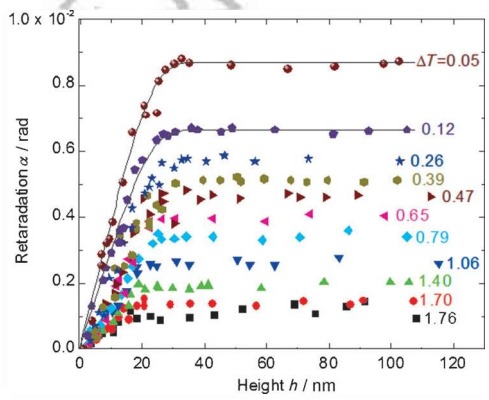


Figure 7. Optical retardation versus height of fiber aperture above the substrate. The different symbols correspond to different temperatures ΔT above T_{NI}.

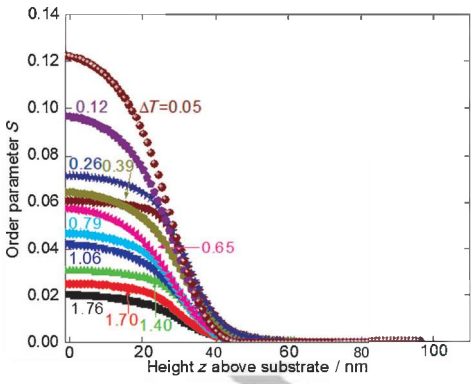


Figure 8. Measured order parameter versus height above the substrate. The different symbols correspond to different temperatures ΔT above T_{NI}.

From Figure 8 we can deduce that that the surface-induced order parameter $S_0 \lesssim 0.12$ at $z = 0$ and that the inverse susceptibility S_0^{-1} versus T is mean-field-like, scaling approximately as $T - T^*$, where T^* is the supercooling limit of the isotropic phase. The magnitude and decay length of S are inconsistent with capillary condensation[57,60,64,65]—this is a different process in which there is a transition to the nematic phase in a confined region—in our system for the temperatures studied. More importantly, we found that $S(z)$ varies slowly with height out to ~10 nm as the fiber is withdrawn (Figure 8). This is substantially different from the conventional wisdom of quasi-exponential decay of order expected for a weak delta-function potential localized at the interface.[56–59] ■■ok?■■Our original interpretation[63] suggested the existence of a nonlocal interaction potential extending out to $z \sim 5$ to 8 nm between the liquid crystal and polymer substrate, in conjunction with a possible breakdown of continuum behavior in the form of molecular cluster formation very close to the substrate. More recently, however, it has been shown theoretically[63] that the small value of the NI interfacial tension results in the renormalization of the repulsive interaction potential due to the thermal fluctuations of the soft NI-interface. This leads to an increase of the equilibrium width of the induced nematic region and the appearance of a shoulder-like orientational order parameter profile, as observed.[63] It was found theoretically that only renormalized short-range[67,68] and thermal pseudo-Casimir interactions[69,70] are essential for this behavior.[66]

An important experimental issue to consider is the effect of the probe on the liquid crystal. As noted above, the rapid but small amplitude motion of the fiber probe does not have a reorienting effect on the director orientation. But does the fiber impose specific boundary conditions on the director? Based on the work in refs. [43,46], Figures 2 and 3 herein, as well as the extracted value of S_0^{-1} from Figure 8 herein, empirically it appears that the orientational alignment at the fiber is degenerate: The order at the fiber aperture corresponds approximately to the order that would be expected in the absence of the fiber. To be sure, this observation is only empirical and requires more investigation. For measurements very close to the substrate, well within the fiber diameter (such as in the experiment immediately preceding), the order at the fiber can be

© 2014 Wiley-VCH Verlag GmbH & Co. KGaA, Weinheim

quite important; further from the fiber it is of less significance. We have performed several other experiments that were analyzed using a similar approximation, with quantitatively very reasonable results.

In the previous two experiments, NSOM was used to obtain orientational information in the *xy* plane and along the *z* axis. Let us examine how NSOM can be applied to create/analyze images in three dimensions.[71] We begin by assuming that the director in the nematic phase is rendered non-uniform either by a patterned surface treatment resulting in a non-uniform easy axis, or by an externally applied field. If the former holds, then the elasticity of the liquid crystal will cause the director orientation to uniformize, that is, become spatially homogeneous, with increasing height *z* above the patterned surface. The goal here is to determine the director profile as a function of *x*, *y*, and *z* with resolution of <100 nm in the *xy* plane and <2 nm along the *z* axis.

As an example, we again scribed a shallow angle herringbone pattern into a polyimide surface.[71] We did this twice: In one case we used a scribed line separation of $d=100$ nm and in the second case a line separation of $d=200$ nm (see Figure 4). The surface was coated with a thin film—a few micrometers—of nematic liquid crystal, and the fiber was immersed into the liquid crystal and lowered until it reached the polyimide substrate. The polarization of the fiber was arranged in such a way that the intensity at the detector would vary approximately linearly with the azimuthal orientation of the liquid crystal on passing from one side of the herringbone to the other. The fiber then was withdrawn to a height $z\sim$ 100 nm, and was rastered in the *xy* plane, during which time the intensity was recorded. After completing a scan, the fiber was withdrawn further and the scanning process was repeated. Seventeen polarized optical images were collected in this manner out to $z=480$ nm. Figure 9 shows a series of images at different heights for the relatively wide $d=200$ nm spacings. The periodic structure in the right-hand side of the patterns corresponds to the topographical variation of the surface that occurs with scribing: The intensity of the transmitted light is larger over the plowed-out lines due to the larger integrated birefringence from the fiber aperture to the bottom of the trough, and is smaller in regions between the scribed lines where there is an apex in the topography. It is particularly interesting that these features appear even at $z=480$ nm. This is discussed later. Instead, for our 3D studies of order we used the data from the more narrowly spaced $d=100$ line separation patterns, and focused on the region where the easy axis, and thus the director, undergoes a spatially rapid change in direction. In this case the fingers that appear in Figure 9 (due to the wide $d=200$ nm spacing between the scribed lines) do not appear for the more narrow $d=100$ nm spacings, and there is a smooth transition of intensity on traversing from orientation of the scribed herringbone to the next.

Initially we intended to build up a director profile iteratively, using the initial scan ($i=1$) near the surface to obtain the director profile at the surface. The image acquired at the next height, that is, slice $i+1$, would be deconvoluted, as we already had measured the director profile at slice *i*; this would

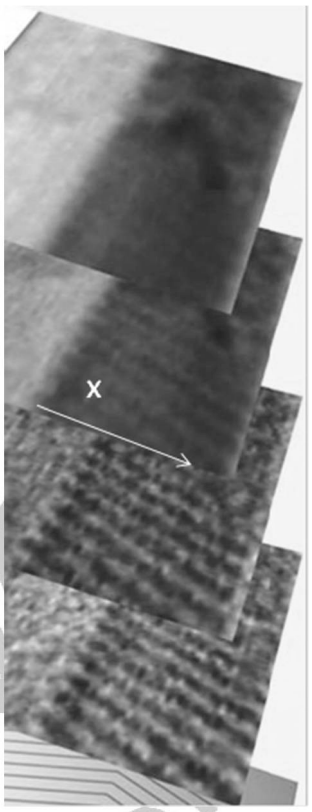


Figure 9. Polarized NSOM images of liquid crystal pentylcyanobiphenyl resting on a herringbone AFM-scribed polyimide surface with scribe lines separated by $d=200$ nm. From top to bottom, the aperture height is $z=480$, 320, 210, and 115 nm above the surface. The bottom image is a cartoon of the scribing pattern. The *x* direction, shown by the arrow, corresponds to the NSOM scanning direction.

then give us the director profile at slice $i+1$. In this manner a 3D director profile could be built up in layers, giving our approach the moniker optical nanotomography. But, as can be seen from Figure 9, there is significant noise in the signal, especially for smaller *z* closer to the surface. As a result, our iterative deconvolution technique tends to introduce significant error beginning at $i=1$, which propagates through the entire analysis. In order to use this approach effectively it would be necessary to use much slower scans, averaging the intensity measured at each point to improve the statistics. Instead, we chose to compare the experimental images obtained with theoretical predictions for the intensity based on continuum elastic theory[1] and using a Berreman 4×4 optical calculation.[72] Figure 10a shows a plot of intensity versus lateral position of the fiber as it traverses two boundaries across the herringbone. Here, the substrate was scribed softly. Apparent from Figure 10 are the effects of optical noise, which tends to be worse closer to the surface, as seen in Figure 10b. From the apparent extrapolation length $L\sim400$ nm observed in Figure 10b, we can estimate the anchoring strength as $W_2\sim(2.5\pm0.8)\times10^{-2}$ erg cm^{-2}.[71] Notice also that the rise and fall of the intensity is sharper in Figure 10b than in 10a: Because of the height of the fiber in Figure 10a, the director is showing the expected uniformation. Thus, although it is gratifying that the optical

© 2014 Wiley-VCH Verlag GmbH & Co. KGaA, Weinheim

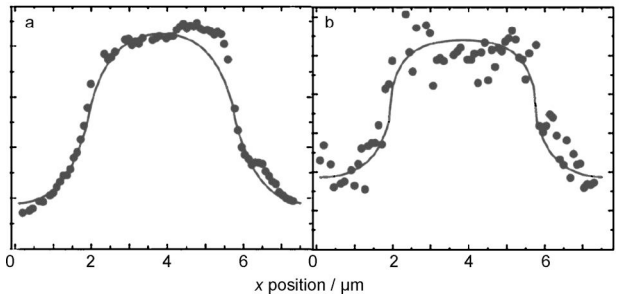


Figure 10. Intensity profile [arbitrary units] versus position x of fiber, where x is as shown in Figure 9. Points represent data and solid lines are theoretical values. a) $z = 480$ nm and b) $z = 115$ nm.

data is consistent with the expected values calculated according to continuum theory, this approach still requires significant refinement and improvement of signal-to-noise before it can be used reliably to measure director profiles in three dimensions.

As noted previously, NSOM data can be used to understand the surface topography.[73] When a surface is treated to provide an easy axis, and the treatment induces a surface topography, the distance between the surface and the fiber aperture maintained at some average fixed height above the surface will vary as the fiber is rastered in the xy plane. In other words, if the topographical period is long, the fiber's average height will vary■■ok?■■. But for sufficiently rapid variation of the topography in space, the fiber can be maintained at a fixed height. As a result, the total optical retardation α will vary with position, as the depth of the birefringent liquid crystal will be larger if the fiber sits above a trough in the topography and smaller if it sits above the apex. Using this idea, we AFM-scribed a polyimide surface by alternatively pushing and pulling from one line to the next.[73] Because the line spacing was $d =$ 200 nm, and pushing and pulling are different operations (pulling plows out a deeper trough), the period of the pattern actually was 400 nm, that is, the distance between successive pulls. The inset in Figure 11 shows an AFM image taken at

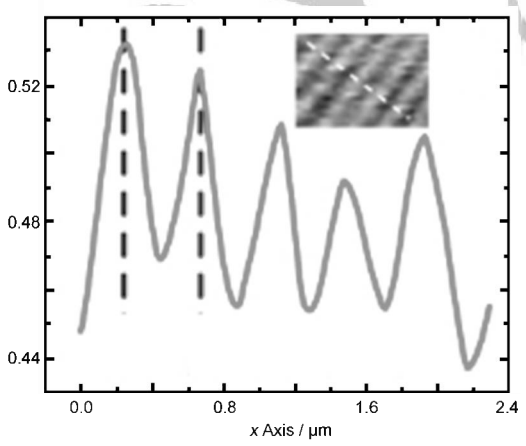


Figure 11. Intensity of NSOM signal across along the dotted line shown in the inset. (Reproduced from ref. [73]. © IOP Publishing, reprinted with permission).

a height $z = 115$ nm and the curve shows the intensity (arbitrary units) along the dotted line in the inset.

We measured the normalized intensity difference $R = (I_{max} - I_{min})/(I_{max} + I_{min})$ between trough and apex as a function of the average aperture height z from 115 to 480 nm. R is large close to the surface, as the surface roughness, which we determined to be $\Delta z \sim 18$ nm by AFM measurements, comprises a larger fraction of the average height of the fiber than it does when the fiber is far above the surface. Figure 12 shows R

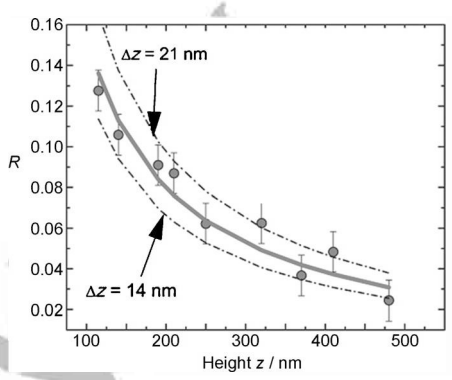


Figure 12. Normalized intensity $R = (I_{max} - I_{min})/(I_{max} + I_{min})$ versus average height of fiber aperture above the surface. The solid line is a one parameter least squares fit ($\Delta z = 17$ nm) of the data to a plane-wave optical-retardation model. The dotted lines show the results of the model assuming a roughness of $\Delta z = 14$ nm and 21 nm. (Reproduced from ref. [73]. © IOP Publishing, reprinted with permission)

versus z. Using only a single parameter Δz, the data were fitted to a plane-wave model for the optical retardation. A best fit was obtained with $\Delta z = (17 \pm 3)$ nm, which is in excellent agreement with the AFM results. Thus, exploiting the birefringence of the liquid crystal, one can obtain nanometer scale resolution of surface roughness from the optical NSOM signal.

Finally, let me turn to another surface-sensitive measurement. With any alignment technique one always encounters a degree of frozen-in orientational disorder, that is, a distribution of easy axis orientations for alignment, which may depend on the structure of the alignment layer and the presence of adsorbed liquid crystal and/or impurity molecules. Nespoulous, et al. have measured such a distribution.[74] Based on the equivalence of the Langevin equation describing Brownian motion[75] and the equations governing the director at the surface,[1] they showed[74] that the resulting spatial correlation function corresponds to an orientational version of quenched disorder,[76] that is, orientational quenched disorder (OQD)[77–79] in which the correlations decay over some characteristic length scale ξ. Although not very important in large-pixel liquid crystal displays, OQD may have profound effects on phase transitions[80] and defect dynamics,[81] and impact the quality and efficiency of microdisplays and energy-related technologies. Moreover, as orientational patterns become more complex and smaller-scale, the consequences of OQD will become more pronounced.

Despite the great success of the Montpellier (France) group in characterizing the quenched disorder,[74] including its corre-

WILEY-VCH Galley Proof

© 2014 Wiley-VCH Verlag GmbH & Co. KGaA, Weinheim

lation length and orientational distribution function, their resolution was diffraction limited, being several hundred micrometers across. Given the much finer resolution inherent in an NSOM probe, we have begun to exploit this approach. We first arranged the polarization in such a way that azimuthal deviations $\Delta\phi$ of the director from the average easy axis—here the easy axis was created by polarized UV alignment—resulted in an intensity change linear in the deviation. The probe was rastered in the *xy* plane inside a thin liquid crystal film at a height of $z \sim 70$ nm. Figure 13 shows a typical pattern obtained over a 30×30 μm square. Figure 14 shows a histogram of the distribution, where the width of the distribution is ~1°.

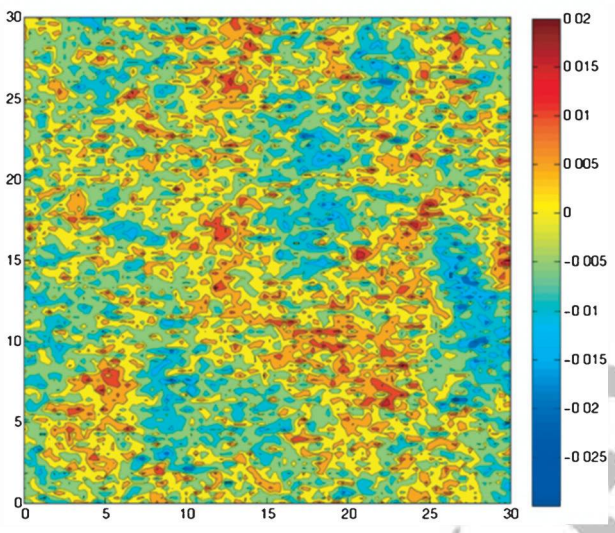


Figure 13. Plot of angular deviation $\Delta\phi$ of director from the average easy axis. $\Delta\phi$ ranges from 0.02 rad (deep red) to −0.03 rad (deep blue); yellow approximately corresponds to $\Delta\phi = 0$. For calibration purposes, it is easiest to create a nearby region with a slightly different, but well characterized, average easy axis orientation.

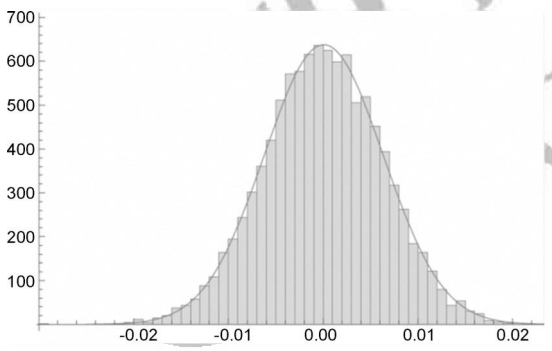


Figure 14. Histogram of angular deviations from average easy axis. Vertical units correspond to the number of NSOM pixels and horizontal units correspond to radians.

From the data in Figure 13, we are able to calculate the Fourier transform of $\Delta\phi(\vec{r})$ to obtain $\Delta\phi(\vec{q})$ and the power spectral density, and then obtain the 2D autocorrelation function $\langle\Delta\phi(0)\Delta\phi(\vec{r})\rangle$, along with a characteristic correlation length $\xi \sim 300$ nm, by inverse Fourier transforming $\Delta\phi(\vec{q})\Delta\phi^*(-\vec{q})$. Although this currently is a work in progress[82] it is clear that NSOM can provide extremely high precision quantitative measurements of the director's spatial behavior.

3. Conclusions

Near-field scanning optical microscopy is an extremely powerful tool with a wide variety of applications. In the liquid crystal field, early static measurements in which the fiber was held a short distance above a liquid crystal film soon gave way to measurements in which the fiber was immersed into the liquid crystal to produce detailed sub-diffraction-limit images of the liquid crystal orientation that could be analyzed quantitatively, as well as dynamic measurements of the liquid crystal response to external stimuli. However, NSOM is not a universal panacea: One needs to be extremely careful with boundary conditions at the fiber surfaces, high-resolution temperature control can be difficult, and perhaps most obvious, inserting a fiber into a smectic or lower-symmetry phase will either severely scramble the liquid crystal order or simply is not possible. Nevertheless, for measurements inside the nematic or isotropic phases, this technique can yield information that otherwise is not possible.

Acknowledgements

Many people were involved in NSOM measurements and analysis in my lab, without whom this work would have been impossible. They are Antonio De Luca, Valentin Barna, Timothy J. Atherton, Giovanni Carbone, Matthew E. Sousa, Hi-Hoon Li, Rolfe G. Petschek, Emanuela Bruno, Yoonseuk Choi, and Joel S. Pendery. I also thank Joel S. Pendery for reading the manuscript. Different aspects of the work described herein were funded by the National Science Foundation's Solid State Chemistry and Condensed Matter Physics programs under grants DMR-0804111 and DMR-1065491, the Department of Energy's Office of Basic Science Materials Chemistry program under grant DE-FG02-01ER45934, the Petroleum Research Fund administered by the American Chemical Society, and the Korean Research Foundation under grant KRF-2007-357-C00034, and the Partner University Fund.

Keywords: imaging · liquid crystals · near-field scanning optical microscopy (NSOM) · optical nanotomography

[1] P. G. DeGennes, J. Prost, *Physics of Liquid Crystals*, Clarendon, Oxford, **1994**.■■publisher ok?■■
[2] P. J. Collings, J. S. Patel, *Handbook of Liquid Crystal Research*, Oxford, New York, **1997**.■■publisher ok?■■
[3] I. Dierking, *Textures of Liquid Crystals*, Wiley, New York, **2003**.
[4] I. I. Smalyukh, S. V. Shiyanovskii, O. D. Lavrentovich, *Chem. Phys. Lett.* **2001**, *336*, 88–96.
[5] I. I. Smalyukh, A. N. Kuzmin, A. V. Kachynski, P. N. Prasad, O. D. Lavrentovich, *Appl. Phys. Lett.* **2005**, *86*, 021913.
[6] V. J. Anderson, E. M. Terentjev, S. P. Meeker, J. Crain, W. C. K. Poon, *Eur. Phys. J. E* **2001**, *4*, 11–20.
[7] K. Miyano, *Phys. Rev. Lett.* **1979**, *43*, 51–54.
[8] W. Chen, L. J. Martinez-Miranda, H. Hsiung, Y. R. Shen, *Phys. Rev. Lett.* **1989**, *62*, 1860–1863.
[9] H. Hsiung, T. Rasing, Y. R. Shen, *Phys. Rev. Lett.* **1986**, *57*, 3065–3068.

© 2014 Wiley-VCH Verlag GmbH & Co. KGaA, Weinheim

[10] C. Rosenblatt, *Phys. Rev. A* **1985**, *32*, 1115 – 1121.
[11] M. Moriyama, N. Mizoshita, T. Yokota, K. Kishimoto, T. Kato, *Adv. Mater.* **2003**, *15*, 1335 – 1338.
[12] H. Qi, T. Hegmann, *J. Mater. Chem.* **2006**, *16*, 4197 – 4205.
[13] R. P. Lemieux, G. B. Schuster, *J. Org. Chem.* **1993**, *58*, 100 – 110.
[14] T. W. Stinson, J. D. Litster, N. A. Clark, *J. Phys.* **1972**, *33*, 69 – 75.■■correct page(s)?■■
[15] I. Musevič, R. Blinc, B. Žeks, C. Filipič, M. Čopič, A. Seppen, P. Wyder, A. Levanyuk, *Phys. Rev. Lett.* **1988**, *60*, 1530 – 1533.
[16] H. Birecki, R. Schaetzing, F. Rondelez, J. D. Litster, *Phys. Rev. Lett.* **1976**, *36*, 1376 – 1379.
[17] M. H. Lu, K. A. Crandall, C. Rosenblatt, *Phys. Rev. Lett.* **1992**, *68*, 3575 – 3578.
[18] M. R. Dodge, R. G. Petschek, C. Rosenblatt, M. E. Neubert, M. E. Walsh, *Phys. Rev. E* **2003**, *68*, 031703.
[19] R. Sigel, *Curr. Opin. Colloid Interface Sci.* **2009**, *14*, 426 – 437.
[20] T. Lee, H. Mundoor, D. G. Gann, T. J. Callahan, I. I. Smalyukh, *Opt. Express* **2013**, *21*, 12129.
[21] R. Pratibha, W. Park, I. Smalyukh, *J. Appl. Phys.* **2010**, *107*, 063511.
[22] D. Engström, R. P. Trivedi, M. Persson, M. Goksör, K. A. Bertness, I. I. Smalyukh, *Soft Matter* **2011**, *7*, 6304 – 6312.
[23] E. H. Synge, *Philos. Mag.* **1928**, *6*, 356 – 362; E. H. Synge, *Philos. Mag.* **1931**, *11*, 65 – 80; E. H. Synge, *Philos. Mag.* **1932**, *13*, 297.■■3rd no page range ok?■■
[24] G. Binnig, H. Rohrer, C. Gerber, E. Weibel, *Phys. Rev. Lett.* **1982**, *49*, 57 – 58.
[25] D. W. Pohl, Eur. Patent 0112401, issued 27/12/, **1982**.
[26] D. W. Pohl, W. Denk, M. Lanz, *Appl. Phys. Lett.* **1984**, *44*, 651 – 653.
[27] A. Lewis, M. Isaacson, A. Harootunian, A. Murray, *Ultramicroscopy* **1984**, *13*, 227 – 231.
[28] A. Harootunian, E. Betzig, M. Isaacson, A. Lewis, *Appl. Phys. Lett.* **1986**, *49*, 674 – 676.
[29] P. J. Moyer, K. Walzer, M. Hietschold, *Appl. Phys. Lett.* **1995**, *67*, 2129 – 2131.
[30] R. L. Williamson, M. J. Miles, *J. Appl. Phys.* **1996**, *80*, 3143 – 3146.
[31] K. Kočevar, I. Muševič, *Phys. Rev. E* **2002**, *65*, 021703.
[32] H. Ade, R. Toledo-Crow, M. Vaez-Iravani, R. J. Spontak, *Langmuir* **1996**, *12*, 231 – 234.
[33] P. S. Ramanujam, N. C. R. Holme, S. Hvilsted, *Appl. Phys. Lett.* **1996**, *68*, 1329 – 1331.
[34] T. Huser, T. Lacoste, H. Heinzelmann, H.-S. Kitzerow, *J. Chem. Phys.* **1998**, *108*, 7876 – 7880.
[35] I. H. Bechtold, F. Batalioto, L. T. Thieghi, B. S. L. Honda, M. Pojar, J. Schoenmaker, A. D. Santos, V. Zucolotto, D. T. Balogh, O. N. Oliveira, E. A. Oliveira, *Phys. Rev. E* **2006**, *74*, 021714.
[36] S. G. Lukishova, A. W. Schmid, *Mol. Cryst. Liq. Cryst.* **2006**, *454*, 15 – 21.
[37] E. Mei, D. A. Higgins, *J. Phys. Chem. A* **1998**, *102*, 7558 – 7563.
[38] E. Mei, D. A. Higgins, *J. Chem. Phys.* **2000**, *112*, 7839 – 7847.
[39] E. Mei, D. A. Higgins, *Appl. Phys. Lett.* **1999**, *75*, 430 – 432.
[40] D. A. Higgins, X. Liao, J. E. Hall, E. Mei, *J. Phys. Chem. B* **2001**, *105*, 5874 – 5882.
[41] J. E. Hall, D. A. Higgins, *J. Phys. Chem. B* **2003**, *107*, 14211 – 14218; J. E. Hall, D. A. Higgins, *J. Phys. Chem. B* **2004**, *108*, 16050 – 16055.
[42] D. A. Higgins, J. E. Hall, A. F. Xie, *Acc. Chem. Res.* **2005**, *38*, 137 – 1445.
[43] T. Tadokoro, T. Saiki, H. Toriumi, *Jpn. J. Appl. Phys.* **2002**, *41*, L152 – L154.
[44] L. Novotny, D. W. Pohl, B. Hecht, *Opt. Lett.* **1995**, *20*, 970 – 972.
[45] F. C. Frank, *Discuss. Faraday Soc.* **1958**, *25*, 19 – 28.
[46] T. Tadokoro, T. Saiki, H. Toriumi, *Jpn. J. Appl. Phys.* **2003**, *42*, L57 – L59.
[47] J. Qin, K. Iwami, N. Umeda, *Jpn. J. Appl. Phys.* **2009**, *48*, 030212.
[48] P. P. Karat, N. V. Madhusudana, *Mol. Cryst. Liq. Cryst.* **1976**, *36*, 51 – 64.
[49] J. Qin, N. Umeda, *Chin. Phys. Lett.* **2007**, *24*, 2906 – 2909.
[50] J. Qin, K. Iwami, N. Umeda, *Appl. Phys. Express* **2008**, *1*, 111501.
[51] V. Vandenbrouck, S. Bardon, M. P. Valignat, A. M. Cazabat, *Phys. Rev. Lett.* **1998**, *81*, 610 – 613.
[52] S. Faetti, M. Gatti, V. Palleschi, T. J. Sluckin, *Phys. Rev. Lett.* **1985**, *55*, 1681 – 1684.
[53] H. Yokoyama, S. Kobayashi, H. Kamei, *J. Appl. Phys.* **1984**, *56*, 2645 – 2654.
[54] Y. Choi, C. Rosenblatt, *Phys. Rev. E* **2010**, *81*, 051708.
[55] D. Davidov, C. R. Safinya, M. Kaplan, S. S. Dana, R. Schaetzing, R. J. Birgeneau, J. D. Litster, *Phys. Rev. B* **1979**, *19*, 1657 – 1663.
[56] K. Miyano, *J. Chem. Phys.* **1979**, *71*, 4108.
[57] P. Sheng, *Phys. Rev. A* **1982**, *26*, 1610 – 1617.
[58] M. B. Feller, W. C. Chen, Y. R. Shen, *Phys. Rev. A* **1991**, *43*, 6778 – 6792.
[59] T. Moses, Y. R. Shen, *Phys. Rev. Lett.* **1991**, *67*, 2033 – 2036.
[60] A. Poniewierski, T. J. Sluckin, *Liq. Cryst.* **1987**, *2*, 281 – 311.
[61] B. Wen, J.-H. Kim, H. Yokoyama, C. Rosenblatt, *Phys. Rev. E* **2002**, *66*, 041502.
[62] X. Liu, D. W. Allender, D. Finotello, *Europhys. Lett.* **2002**, *59*, 848 – 854.
[63] J.-H. Lee, T. J. Atherton, V. Barna, A. De Luca, E. Bruno, R. G. Petschek, C. Rosenblatt, *Phys. Rev. Lett.* **2009**, *102*, 167801.
[64] H. Yokoyama, S. Kobayashi, H. Kamei, *J. Appl. Phys.* **1987**, *61*, 4501 – 4518.
[65] K. Kočevar, A. Borstnik, I. Musevič, S. Žumer, *Phys. Rev. Lett.* **2001**, *86*, 5914 – 5917.
[66] E. Pikina, C. Rosenblatt, *Eur. Phys. J. E* **2012**, *35*, 87.
[67] D. S. Fisher, D. A. Huse, *Phys. Rev. B* **1985**, *32*, 247 – 256.
[68] J. N. Israelachvili, *Intermolecular and Surface Forces*, Academic, New York, **1985**.■■Academic Press?■■
[69] A. Ajdari, L. Peliti, J. Prost, *Phys. Rev. Lett.* **1991**, *66*, 1481 – 1484.
[70] P. Ziherl, A. Sarlah, S. Zumer, *Phys. Rev. E* **1998**, *58*, 602 – 609.
[71] A. De Luca, V. Barna, T. J. Atherton, G. Carbone, M. E. Sousa, C. Rosenblatt, *Nat. Phys.* **2008**, *4*, 869 – 872.
[72] D. W. Berreman, *J. Opt. Soc. Am.* **1972**, *62*, 502 – 510.
[73] V. Barna, A. De Luca, C. Rosenblatt, *Nanotechnology* **2008**, *19*, 325709.
[74] M. Nespoulous, C. Blanc, M. Nobili, *Phys. Rev. Lett.* **2010**, *104*, 097801.
[75] P. Langevin, *C. R. Acad. Sci.* **1908**, *146*, 530 – 533.
[76] A. Weinrib, B. I. Halperin, *Phys. Rev. B* **1983**, *27*, 413 – 427.
[77] T. Bellini, M. Buscaglia, C. Chiccoli, F. Mantegazza, P. Pasini, C. Zannoni, *Phys. Rev. Lett.* **2000**, *85*, 1008 – 1101.
[78] D. K. Shenoy, J. V. Selinger, K. A. Grüneberg, J. Naciri, R. Shashidhar, *Phys. Rev. Lett.* **1999**, *82*, 1716 – 1719.
[79] L. Radzihovsky, Q. Zhang, *Phys. Rev. Lett.* **2009**, *103*, 167802.
[80] L. Petridis, E. Terentjev, *Phys. Rev. E* **2006**, *74*, 051707.
[81] C. Blanc, S. SvenŠek, S. žumer, M. Nobili, *Phys. Rev. Lett.* **2005**, *95*, 097802.
[82] J. S. Pendery, C. Rosenblatt, unpublished.

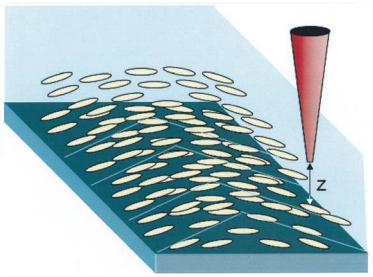
Received: October 23, 2013
Published online on ■■ ■■, 2014

© 2014 Wiley-VCH Verlag GmbH & Co. KGaA, Weinheim

*C. Rosenblatt**

■■–■■

Optical Imaging of Liquid Crystals at the Nanoscale



Coming closer: Near-field scanning optical microscopy (NSOM) is exploited to provide three-dimensional structure and dynamic information about liquid crystals at scales as small as a few nanometers. (Image courtesy of Prof. Antonio De Luca. After V. Vandenbrouck, S. Bardon, M. P. Valignat, A. M. Cazabat, *Phys. Rev. Lett.* **1998**, *81*, 610–613. © American Physical Society, reprinted with permission.)■■ok?■■

Get 3D #structure and #dynamic information on #liquid #crystals at the #nanoscale by #NSOM SPACE RESERVED FOR IMAGE AND LINK

ChemPhysChem is piloting a social networking feature involving Twitter, an online microblogging service that enables its users to send and read text-based messages of up to 140 characters, known as "tweets". Please check the pre-written tweet in the galley proofs for accuracy. Should you or your institute have a Twitter account, please let us know the appropriate username (e.g., @ChemPhysChem), and we will do our best to include this information in the tweet. This tweet will be posted to the journal's Twitter account upon online publication of your article.

WILEY-VCH Galley Proofs

© 2014 Wiley-VCH Verlag GmbH & Co. KGaA, Weinheim